Mechanical Systems and Signal Processing 241 (2025) 113405

Contents lists available at ScienceDirect

Mechanical Systems and Signal Processing

journal homepage: www.elsevier.com/locate/ymssp

Full Length Article

# Hyper-viscoelastic dynamic modeling and analysis for soft dielectric elastomer actuators

Liwen Zhang [a], Xiaotian Shi [b,c], Guoying Gu [b,c], Jiang Zou [b,c,**], Jinyang Liu [a,*]

[a] Department of Engineering Mechanics, School of Ocean and Civil Engineering, Shanghai Jiao Tong University, Shanghai 200240, PR China
[b] The State Key Laboratory of Mechanical System and Vibration, Shanghai Jiao Tong University, Shanghai 200240, PR China
[c] The Robotic Institute, School of Mechanical Engineering, Shanghai Jiao Tong University, Shanghai 200240, PR China

ARTICLE INFO

Communicated by Olga Fink

*Keywords:*
Dynamic modeling
Dielectric elastomer actuator
Viscoelasticity
Arbitrary shaped flexible structure
Geometric nonlinearity

ABSTRACT

For the dielectric elastomer actuators (DEAs) with high-frequency excitations and large deformations, it is full of challenges to accurately describe their continuum dynamic responses due to the viscoelastic effect and geometric nonlinearity. The absolute nodal coordinate formulation (ANCF) possesses notable advantages in precisely depicting the rigid-body motions and large deformations of the DEAs. In this paper, a novel ANCF hyper-viscoelastic solid element for arbitrary shaped DEAs is developed, where the accuracy of predicting viscoelasticity is improved by adding more viscoelastic units to a two-part constitutive viscoelastic model. The volumetric locking problem of incompressible material is effectively avoided by using high-order interpolation functions. Firstly, the homogeneous deformations of a dielectric elastomer block are predicted with the proposed model and verified with the analytical solutions. Secondly, the proposed model is proved to be applicable to the DEAs with complex shapes by studying the dynamic response of a three-dimensional torsional DEA. Subsequently, the effectiveness of the proposed model under a wide frequency range is demonstrated through the experiments and dynamic simulations of a rolled DEA. The numerical results show that the hysteresis effect and creep of the rolled DEA are predicted more precisely with the proposed model than those obtained with only one viscoelastic unit. Finally, the effect of changing geometric parameters and applying different loading voltages on the actuation properties of a rolled DEA are further analyzed. The proposed viscoelastic dynamic model can be implemented effectively in the design of a complex DEA with fast responsiveness and high deformability.

## 1. Introduction

Dielectric elastomer (DE) material is an electroactive polymer material that was gradually developed in the 1990s. It is characterized by its large deformation that the applied voltage can make it expand horizontally and shrink vertically at the same time, as illustrated in Fig. 1. Because of its good deformability stimulated by electric energy, DE becomes a heated research topic among researchers and has been widely used in the fields like biomedicine, intelligent robots and wearable devices [1–3]. It is also found that DE

* Corresponding author at: Department of Engineering Mechanics, School of Ocean and Civil Engineering, Shanghai Jiao Tong University, Shanghai 200240, PR China.
** Corresponding author at: The State Key Laboratory of Mechanical System and Vibration, Shanghai Jiao Tong University, Shanghai 200240, PR China; The Robotic Institute, School of Mechanical Engineering, Shanghai Jiao Tong University, Shanghai 200240, PR China.
*E-mail addresses:* zoujiang@sjtu.edu.cn (J. Zou), liujy@sjtu.edu.cn (J. Liu).

https://doi.org/10.1016/j.ymssp.2025.113405
Received 30 April 2025; Received in revised form 19 August 2025; Accepted 21 September 2025
Available online 14 October 2025

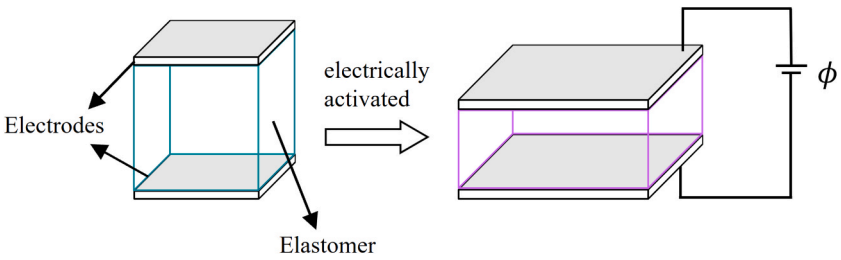


**Fig. 1.** The voltage-induced deformation of a dielectric elastomer membrane.

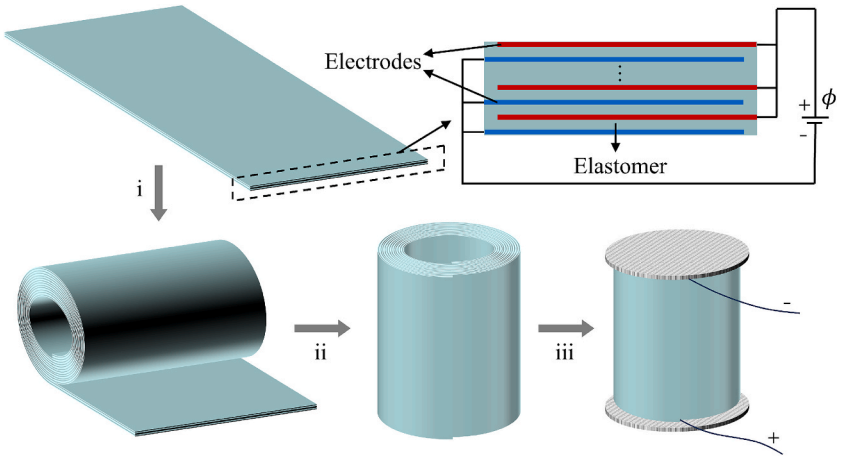


**Fig. 2.** The rolling process of a rolled DEA. (i-ii) Rolling the DE membrane into a tubular shape. (iii) Glueing flat caps to the ends and applying voltage in the radial (thickness) direction.

exhibits many other notable features, such as large energy densities, quick response to voltages and obvious viscoelasticity. These characteristics make DE particularly attractive for soft actuator applications especially in harsh environments. Therefore, it is of great significance to conduct further studies on DE's electrodeformation principle and designs, which can advance the development and application of DEAs.

In order to improve the response speed and deformation of dielectric elastomer actuator (DEA) under electrical load, researchers have designed many different configurations of DEAs, such as the stacked DEA [4–6], the foldable DEA [7,8], the spiral DEA [9] and the annular DEA [10,11]. The rolled DEA is made by bending the dielectric elastomer membrane into a tubular shape, as seen in Fig. 2, usually supported by a compressed spring inside [12–14]. Without outer frame and any spring core inside, the rolled DEA will have a longer service life and smaller unidirectional actuation elongation [15,16]. The centrally symmetrical configuration of the rolled DEA can generate more mechanical energy by converting its biaxial stretching into a large uniaxial deformation subject to the applied voltage.

Associated with nonlinear electrostatics, hyper-viscoelastic membrane behavior and geometric nonlinearities, it is challenging to precisely model the DEAs and performing numerical simulations. In the previous researches, the static characteristics of the DEAs were fully studied [21]. Recently, some efficient dynamic models have been developed to model the DEAs using few degrees of freedom [17–19], such as the physical model for the dielectric electroactive polymer (DEAP) actuator system coupling both electrical and mechanical dynamics [20] and the nonlinear electromechanical model for the PolyPower DEA based on an electric circuit model [22]. In these researches, the stretches in the main directions are usually used to describe the deformation of the DEAs with typical configurations such as spherical [40], rectangular [41], tubular [42], and circular [43] shapes. To obtain more details of 3D deformed configuration and achieve more accurate results, the nonlinear finite element method is further developed for the DEAs [23–25]. Compared with the traditional finite element method, the absolute nodal coordinate formulation (ANCF) possesses notable advantages in precisely depicting the rigid-body motions and large deformations of flexible body. Recently, several researches of the DEAs based on ANCF have been carried out [26,27], where the viscoelastic effects are hardly addressed.

As a kind of polymer material, the DE material has significant viscoelasticity effect such as viscoelastic creep under constant voltage signal [28] and hysteresis subject to cyclic loading voltages [29,30]. In the previous research, there is a simplified way to describe the viscoelasticity of DEAs by making use of an experiment-based identification, without explicit use of a viscoelastic model [31]. Viscoelastic theories based on the Bergstrom-Boyce model has been generalized to investigate both anisotropy and viscoelasticity of DE membrane [32–34]. Based on the rheological model, several analytical models accounting viscoelastic effects have been presented to describe the unconstrained configurations of DEAs involving homogeneous deformations [35–37]. By adding more parallel

viscoelastic units to the conventional model, the viscoelastic effects of DEAs can be predicted more accurately [39]. Furthermore, a computationally efficient numerical framework is also developed to capture the viscoelastic behaviors and inhomogeneous deformations of the DEAs with complex geometries [38].

In order to precisely predict the viscoelastic behaviors of the DEAs with fast responsiveness and inhomogeneous deformations, it is crucial to develop a general visco-hyperelastic dynamic model with multiple viscoelastic units, which is applicable to DEAs in arbitrary shapes.

In the following section, a viscoelastic dynamic model with multiple viscoelastic units for the arbitrary shaped DEAs is established first based on the ANCF method, and then dynamic equations of the whole system are derived according to the Hamilton's principle. Section 3 describes the procedure of solving the dynamic equations by applying the generalized α method. In Section 4, the homogeneous deformations of a dielectric elastomer block are simulated and verified with the analytical solutions. In Section 5, the proposed model is proved to be applicable to the DEAs with complex shapes by investigating the dynamic performance of a three-dimensional torsional DEA. In Section 6, the effectiveness of the developed model is validated experimentally by performing dynamic simulations of a rolled DEA subject to cyclic loading voltage. Subsequently, the influence of different geometric parameters and loading histories on the actuation properties of the rolled DEA are further analyzed. Finally, conclusions of the investigation will be summarized.

## 2. Dynamic modeling of the DEA

### 2.1. ANCF solid element of DEA

For flexible systems with large deformation, geometric nonlinearity needs to be considered in the modeling process. Currently, dynamic modeling methods for large deformation problems mainly include three types: absolute nodal coordinate formulation (ANCF), corotational method and geometrically exact formulation. In this investigation, absolute nodal coordinate formulation (ANCF) is used for dynamic modeling of the DEA [26], in which the absolute coordinates of the nodes in the inertial coordinate system and their gradients are used as generalized coordinates to describe the configuration of the flexible system.

As seen in Fig. 3, *O-**XYZ*** is the inertial coordinate system. For a solid element with 8 nodes, the reference configuration is defined as $\Omega_0$, and the base vectors of the reference material coordinate system are $\boldsymbol{a}_c (c = 1,2,3)$. The current configuration at time $t$ is defined as $\Omega$, and the base vectors of the current material coordinate system are $\boldsymbol{A}_c (c = 1,2,3)$. To evolve the system dynamic equations of the DEAs in arbitrary shapes, the absolute nodal position vectors and their gradients with respect to the material coordinates are denoted as generalized coordinates.

In the current configuration, the absolute position vector of an arbitrary material point is expressed as

$$\boldsymbol{r} = \boldsymbol{S}\boldsymbol{q}_e \tag{1}$$

$$\boldsymbol{S} = [\boldsymbol{S}_1 \quad \boldsymbol{S}_2 \quad \cdots \quad \boldsymbol{S}_8] \tag{2}$$

$$\boldsymbol{S}_i = [s_{i1} \quad s_{i2} \quad s_{i3} \quad s_{i4}]\boldsymbol{I} \tag{3}$$

where $\boldsymbol{S}$ is the shape function matrix, $s_{il}$ $(l = 1,2,3,4)$ are provided in Appendix 1 and the vector of element coordinates $\boldsymbol{q}_e$ is given by

$$\boldsymbol{q}_e = [(\boldsymbol{q}_e^1)^{\mathrm{T}} \quad (\boldsymbol{q}_e^2)^{\mathrm{T}} \quad \cdots \quad (\boldsymbol{q}_e^8)^{\mathrm{T}}]^{\mathrm{T}} \tag{4}$$

To alleviate the volumetric locking problem of incompressible material, gradient coordinates are included in each node of the element, the coordinate vector of each node takes the form

$$\boldsymbol{q}_e^i = [(\boldsymbol{r}^i)^{\mathrm{T}} \quad (\boldsymbol{r}_\xi^i)^{\mathrm{T}} \quad (\boldsymbol{r}_\eta^i)^{\mathrm{T}} \quad (\boldsymbol{r}_\zeta^i)^{\mathrm{T}}]^{\mathrm{T}} \tag{5}$$

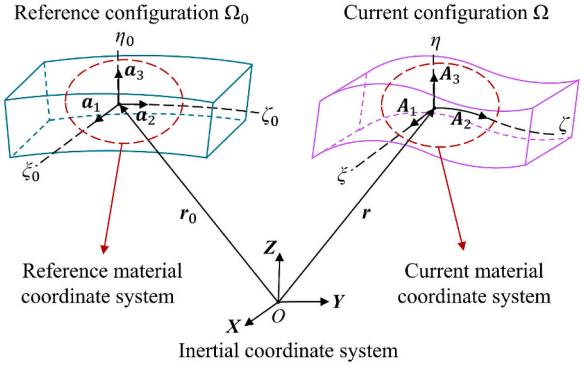


**Fig. 3.** Configuration of the DE solid element.

where $\boldsymbol{r}^i$ is the absolute position vector of node $i$ ($i = 1, 2, \cdots, 8$) and $\boldsymbol{r}_j^i$ is the partial derivatives of $\boldsymbol{r}^i$ with respect to the material coordinate $j$ ($j = \xi, \eta, \zeta$).

The deformation gradient with respect to the material coordinates is defined as

$$\boldsymbol{F}_c = [\boldsymbol{r}_\xi \quad \boldsymbol{r}_\eta \quad \boldsymbol{r}_\zeta] = [\boldsymbol{S}_\xi \boldsymbol{q}_e \quad \boldsymbol{S}_\eta \boldsymbol{q}_e \quad \boldsymbol{S}_\zeta \boldsymbol{q}_e], \tag{6}$$

where $\boldsymbol{r}_\xi = \partial \boldsymbol{r}/\partial \xi$, $\boldsymbol{r}_\eta = \partial \boldsymbol{r}/\partial \eta$, $\boldsymbol{r}_\zeta = \partial \boldsymbol{r}/\partial \zeta$, $\boldsymbol{S}_\xi = \partial \boldsymbol{S}/\partial \xi$, $\boldsymbol{S}_\eta = \partial \boldsymbol{S}/\partial \eta$, $\boldsymbol{S}_\zeta = \partial \boldsymbol{S}/\partial \zeta$.

In the reference configuration, the absolute position vector is expressed as $\boldsymbol{r}_0 = \boldsymbol{S}\boldsymbol{q}_{e0} = [x \quad y \quad z]^{\mathrm{T}}$ and the deformation gradient with respect to $\boldsymbol{r}_0$ is given by

$$\boldsymbol{F} = [\boldsymbol{r}_x \quad \boldsymbol{r}_y \quad \boldsymbol{r}_z] = [\boldsymbol{S}_x \boldsymbol{q}_e \quad \boldsymbol{S}_y \boldsymbol{q}_e \quad \boldsymbol{S}_z \boldsymbol{q}_e], \tag{7}$$

where $\boldsymbol{r}_x = \partial \boldsymbol{r}/\partial x$, $\boldsymbol{r}_y = \partial \boldsymbol{r}/\partial y$, $\boldsymbol{r}_z = \partial \boldsymbol{r}/\partial z$, $\boldsymbol{S}_x = \partial \boldsymbol{S}/\partial x$, $\boldsymbol{S}_y = \partial \boldsymbol{S}/\partial y$, $\boldsymbol{S}_z = \partial \boldsymbol{S}/\partial z$.

The transformation between $\boldsymbol{F}$ and $\boldsymbol{F}_c$ is realized by

$$\boldsymbol{F} = \boldsymbol{F}_c \left( \frac{\partial \boldsymbol{r}_0}{\partial \boldsymbol{\rho}} \right)^{-1} \tag{8}$$

where the current material coordinate vector is defined as $\boldsymbol{\rho} = [\xi \quad \eta \quad \zeta]^{\mathrm{T}}$ and

$$\frac{\partial \boldsymbol{r}_0}{\partial \boldsymbol{\rho}} = [\boldsymbol{r}_{0\xi} \quad \boldsymbol{r}_{0\eta} \quad \boldsymbol{r}_{0\zeta}] = [\boldsymbol{S}_\xi \boldsymbol{q}_{e0} \quad \boldsymbol{S}_\eta \boldsymbol{q}_{e0} \quad \boldsymbol{S}_\zeta \boldsymbol{q}_{e0}] \tag{9}$$

$$\left( \frac{\partial \boldsymbol{r}_0}{\partial \boldsymbol{\rho}} \right)^{-1} = [\boldsymbol{S}_\xi \boldsymbol{q}_{e0} \quad \boldsymbol{S}_\eta \boldsymbol{q}_{e0} \quad \boldsymbol{S}_\zeta \boldsymbol{q}_{e0}]^{-1} = \begin{bmatrix} \xi_x & \xi_y & \xi_z \\ \eta_x & \eta_y & \eta_z \\ \zeta_x & \zeta_y & \zeta_z \end{bmatrix} \tag{10}$$

Based on Eq. (6)-(10), $\boldsymbol{S}_x$, $\boldsymbol{S}_y$, $\boldsymbol{S}_z$ are further evolved

$$\begin{aligned} \boldsymbol{S}_x &= \boldsymbol{S}_\xi \xi_x + \boldsymbol{S}_\eta \eta_x + \boldsymbol{S}_\zeta \zeta_x, \\ \boldsymbol{S}_y &= \boldsymbol{S}_\xi \xi_y + \boldsymbol{S}_\eta \eta_y + \boldsymbol{S}_\zeta \zeta_y, \\ \boldsymbol{S}_z &= \boldsymbol{S}_\xi \xi_z + \boldsymbol{S}_\eta \eta_z + \boldsymbol{S}_\zeta \zeta_z. \end{aligned} \tag{11}$$

Denoting the electric potential and its gradients of the material point as $\varphi$, and its gradients as $\varphi_x = \partial \varphi/\partial x$, $\varphi_y = \partial \varphi/\partial y$, $\varphi_z = \partial \varphi/\partial z$, the nominal electric field $\boldsymbol{E}$ is given as

$$\boldsymbol{E} = [\varphi_x \quad \varphi_y \quad \varphi_z]^{\mathrm{T}} \tag{12}$$

### 2.2. Viscoelastic model with multiple spring-dashpot units

As a polymer material, the DE materials have significant viscoelasticity. Commonly, the viscoelasticity of DEAs is represented with a two-part constitutive model with a single spring element in parallel to one spring-dashpot unit. In this paper, more parallel viscoelastic units are added to the two-part constitutive model, which can help in predicting the viscoelastic effects of DEAs more accurately. As shown in Fig. 4, a single spring element is used to model the elastic equilibrium response, which is in parallel to multiple spring-dashpot units representing the viscous responses of DEAs.

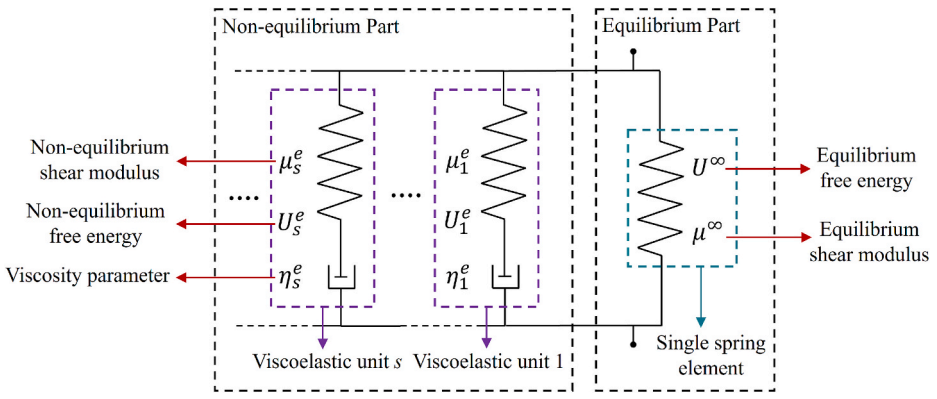


**Fig. 4.** The viscoelastic model with a single spring element in parallel to multiple spring-dashpot units.

In this paper, the equilibrium free energy function $U^{\infty}$ and the non-equilibrium free energy function $U_s^e$ for viscoelastic unit $s$ are both characterized by the Gent model, which can precisely describe the stiffening phenomenon of DEAs in large deformations. The equilibrium shear modulus, bulk modulus and limiting stretch parameter are presented by $\mu^{\infty}$, $K^{\infty}$, and $I_{\lim}^{\infty}$, respectively, and the non-equilibrium shear modulus, bulk modulus and limiting stretch parameter of the viscoelastic unit $s$ are presented by $\mu_s^e$, $K_s^e$, and $(I_{\lim})_s^e$, respectively. Viscosity parameter of viscoelastic unit $s$ is denoted as $\eta_s^e$. For each viscoelastic unit, $\eta^e$, $\mu^e$, $K^e$ and $I_{\lim}^e$ are used to facilitate the derivation of the following formulations.

Defining $\boldsymbol{F}^e$ and $\boldsymbol{F}^v$ as the elastic and viscous components of the deformation gradient, respectively, the total deformation gradient is composed of two parts as $\boldsymbol{F} = \boldsymbol{F}^e\boldsymbol{F}^v$. Therefore, elastic component of the deformation gradient can be written in the form of $\boldsymbol{F}^e = \boldsymbol{F}(\boldsymbol{F}^v)^{-1}$. Denoting the viscous right Cauchy strain tensor as

$$\boldsymbol{C}^v = (\boldsymbol{F}^v)^{\mathrm{T}}\boldsymbol{F}^v \tag{13}$$

the elastic component of the right Cauchy strain tensor is obtained as

$$\boldsymbol{C}^e = (\boldsymbol{F}^e)^{\mathrm{T}}\boldsymbol{F}^e = (\boldsymbol{F}^v)^{-\mathrm{T}}\boldsymbol{C}(\boldsymbol{F}^v)^{-1} \tag{14}$$

where the right Cauchy-Green tensor $\boldsymbol{C}$ is expressed as $\boldsymbol{C} = \boldsymbol{F}^{\mathrm{T}}\boldsymbol{F}$. Considering Eq. (7) and Eq. (14), the traces of $\boldsymbol{C}$ and $\boldsymbol{C}^e$ can also be obtained as

$$I_1 = \mathrm{tr}(\boldsymbol{C}) = \boldsymbol{q}_e^{\mathrm{T}}(\boldsymbol{S}_x^{\mathrm{T}}\boldsymbol{S}_x + \boldsymbol{S}_y^{\mathrm{T}}\boldsymbol{S}_y + \boldsymbol{S}_z^{\mathrm{T}}\boldsymbol{S}_z)\boldsymbol{q}_e \tag{15}$$

$$I_1^e = \mathrm{tr}(\boldsymbol{C}^e) = \boldsymbol{q}_e^{\mathrm{T}}\boldsymbol{B}\boldsymbol{q}_e \tag{16}$$

where

$$\begin{aligned}\boldsymbol{B} = {} & C_{11}^{v-1}\boldsymbol{S}_x^{\mathrm{T}}\boldsymbol{S}_x + C_{12}^{v-1}\boldsymbol{S}_x^{\mathrm{T}}\boldsymbol{S}_y + C_{13}^{v-1}\boldsymbol{S}_x^{\mathrm{T}}\boldsymbol{S}_z \\ & + C_{21}^{v-1}\boldsymbol{S}_y^{\mathrm{T}}\boldsymbol{S}_x + C_{22}^{v-1}\boldsymbol{S}_y^{\mathrm{T}}\boldsymbol{S}_y + C_{23}^{v-1}\boldsymbol{S}_y^{\mathrm{T}}\boldsymbol{S}_z \\ & + C_{31}^{v-1}\boldsymbol{S}_z^{\mathrm{T}}\boldsymbol{S}_x + C_{32}^{v-1}\boldsymbol{S}_z^{\mathrm{T}}\boldsymbol{S}_y + C_{33}^{v-1}\boldsymbol{S}_z^{\mathrm{T}}\boldsymbol{S}_z.\end{aligned} \tag{17}$$

in which $C_{IJ}^{v-1}$ is an element of $(\boldsymbol{C}^v)^{-1}$, and the derivation of $\boldsymbol{B}$ is derived in Appendix 2 in detail.

Based on Eq. (7), the determinant of the deformation gradient is derived as $J = \det(\boldsymbol{F})$. Employing the determinants of the elastic as $J^e$ and viscous components of the deformation gradient as $J^v = \det(\boldsymbol{F}^v) = \sqrt{\det(\boldsymbol{C}^v)}$, the determinant of the elastic component of the deformation gradient is derived as $J^e = J/J^v$.

To capture the particular strain-stiffening effect of DEAs, the incompressible Gent model of hyperelasticity is adopted to derive the equilibrium free energy

$$\begin{aligned}U_e^{\infty} = {} & \int_V \left[ -\frac{1}{2}\mu^{\infty} I_{\lim}^{\infty} \ln\left(1 - \frac{J^{-2/3}I_1 - 3}{I_{\lim}^{\infty}}\right)\right] \mathrm{d}V \\ & + \int_V \left[\frac{1}{2}K^{\infty}(J-1)^2 - \frac{1}{2}\varepsilon J\boldsymbol{E}^{\mathrm{T}}\boldsymbol{C}^{-1}\boldsymbol{E}\right] \mathrm{d}V\end{aligned} \tag{18}$$

and the non-equilibrium free energy of each viscoelastic unit is written as

$$\begin{aligned}U_e^e = {} & \int_V \left[ -\frac{1}{2}\mu^e I_{\lim}^e \ln\left(1 - \frac{(J^e)^{-2/3}I_1^e - 3}{I_{\lim}^e}\right)\right] \mathrm{d}V \\ & + \int_V \left[\frac{1}{2}K^e(J^e-1)^2\right] \mathrm{d}V\end{aligned} \tag{19}$$

where the limiting stretch parameter $I_{\lim}^{\infty}$ and $I_{\lim}^e$ reflect the limiting chain extensibility of rubber networks of the DEs, which can reduce the Gent model to the neo-Hookean model in the limit of $I_{\lim}^{\infty} \to \infty$ [45].

Hence, the free energy of element $e$ can be derived as

$$U_e = U_e^{\infty} + \sum_{s=1}^{nv} (U_e^e)_s \tag{20}$$

where $nv$ is the total number of viscoelastic units.

### 2.3. Formulation of nonlinear dynamic equations

According to Hamilton's principle, the variational equation of the system is obtained as

$$\delta W^{\mathrm{iner}} - \delta U + \delta W^{\mathrm{ext}} = 0 \tag{21}$$

**Table 1**
Relationships between the variables of element $e$ and the variables of the system.

| | Element $e$ | System | Relationship |
|---|---|---|---|
| Generalized coordinates | $\boldsymbol{q}_e$ | $\boldsymbol{q}$ | $\boldsymbol{q}_e = \boldsymbol{B}_e\boldsymbol{q}$ |
| Mass matrix | $\boldsymbol{M}_e$ | $\boldsymbol{M}$ | $\boldsymbol{M} = \sum_{e=1}^{ne}\boldsymbol{B}_e^{\mathrm{T}}\boldsymbol{M}_e\boldsymbol{B}_e$ |
| Generalized external force | $\boldsymbol{Q}_e^{\mathrm{ext}}$ | $\boldsymbol{Q}^{\mathrm{ext}}$ | $\boldsymbol{Q}^{\mathrm{ext}} = \sum_{e=1}^{ne}\boldsymbol{B}_e^{\mathrm{T}}\boldsymbol{Q}_e^{\mathrm{ext}}$ |
| Generalized internal force | $\boldsymbol{Q}_e^{\mathrm{int}}$ | $\boldsymbol{Q}^{\mathrm{int}}$ | $\boldsymbol{Q}^{\mathrm{int}} = \sum_{e=1}^{ne}\boldsymbol{B}_e^{\mathrm{T}}\boldsymbol{Q}_e^{\mathrm{int}}$ |
| Free energy | $U_e$ | $U$ | $U = \sum_{e=1}^{ne}U_e$ |

where the virtual work of inertial force and the external force of the system are expressed as

$$\delta W^{\mathrm{iner}} = -\delta\boldsymbol{q}^{\mathrm{T}}\boldsymbol{M}\ddot{\boldsymbol{q}},\ \delta W^{\mathrm{ext}} = \delta\boldsymbol{q}^{\mathrm{T}}\boldsymbol{Q}^{\mathrm{ext}} \tag{22}$$

and the variation the free energy of the system is given by

$$\delta U = \delta\boldsymbol{q}^{\mathrm{T}}\boldsymbol{Q}^{\mathrm{int}} \tag{23}$$

where $\boldsymbol{Q}^{\mathrm{int}}$ and $\boldsymbol{Q}^{\mathrm{ext}}$ are the generalized internal force vector and the generalized external force vector, respectively.

Defining a conversion matrix as $\boldsymbol{B}_e$, the relationships between the variables of element $e$ ($e = 1 \sim ne$) and corresponding variables of the whole system are listed in Table 1.

For element $e$, according to the rheological model in Fig. 4, the element internal force vector is denoted as

$$\boldsymbol{Q}_e^{int} = \boldsymbol{Q}_e^{\infty} + \sum_{s=1}^{nv}(\boldsymbol{Q}_e^{v})_s \tag{24}$$

where $\boldsymbol{Q}_e^{\infty}$ and $(\boldsymbol{Q}_e^{v})_s$ are derived from the equilibrium free energy and the non-equilibrium free energy, respectively.

For each elastic and viscoelastic unit, the expressions of $\boldsymbol{Q}_e^{\infty}$ and $\boldsymbol{Q}_e^{v}$ are given by

$$\begin{aligned}\boldsymbol{Q}_e^{\infty} = &\int_V \frac{1}{2}\mu^{\infty}\left(1-\frac{J^{-2/3}I_1-3}{I_{\lim}^{\infty}}\right)^{-1}\left[J^{-2/3}\left(\frac{\partial I_1}{\partial\boldsymbol{q}_e}\right)^{\mathrm{T}}\right]\mathrm{d}V\\ &-\int_V \frac{1}{2}\mu^{\infty}\left(1-\frac{J^{-2/3}I_1-3}{I_{\lim}^{\infty}}\right)^{-1}\left[\frac{2}{3}J^{-5/3}\left(\frac{\partial J}{\partial\boldsymbol{q}_e}\right)^{\mathrm{T}}I_1\right]\mathrm{d}V\\ &+\int_V K^{\infty}(J-1)\left(\frac{\partial J}{\partial\boldsymbol{q}_e}\right)^{\mathrm{T}}\mathrm{d}V-\int_V \frac{\varepsilon}{2}(\boldsymbol{E}^{\mathrm{T}}\boldsymbol{C}^{-1}\boldsymbol{E})\left(\frac{\partial J}{\partial\boldsymbol{q}_e}\right)^{\mathrm{T}}\mathrm{d}V\\ &-\int_V \frac{\varepsilon}{2}J\sum_I\sum_J E_I E_J\left(\frac{\partial C_{IJ}^{-1}}{\partial\boldsymbol{q}_e}\right)^{\mathrm{T}}\mathrm{d}V,\end{aligned} \tag{25}$$

$$\begin{aligned}\boldsymbol{Q}_e^{v} = &\int_V \frac{\mu^e}{2}\left(1-\frac{(J^e)^{-\frac{2}{3}}I_1^e-3}{I_{\lim}^e}\right)^{-1}\left[(J^e)^{-\frac{2}{3}}\left(\frac{\partial I_1^e}{\partial\boldsymbol{q}_e}\right)^{\mathrm{T}}\right]\mathrm{d}V\\ &-\int_V \frac{\mu^e}{2}\left(1-\frac{(J^e)^{-\frac{2}{3}}I_1^e-3}{I_{\lim}^e}\right)^{-1}\left[\frac{2(J^e)^{-\frac{5}{3}}}{3J^v}\left(\frac{\partial J}{\partial\boldsymbol{q}_e}\right)^{\mathrm{T}}I_1^e\right]\mathrm{d}V\\ &+\int_V K^e(J^e-1)\frac{1}{J^v}\left(\frac{\partial J^e}{\partial\boldsymbol{q}_e}\right)^{\mathrm{T}}\mathrm{d}V,\end{aligned} \tag{26}$$

and the derivatives of $\boldsymbol{Q}_e^{\infty}$ and $\boldsymbol{Q}_e^{v}$ with respect to $\boldsymbol{q}_e$ are provided in Appendix 3.

Therefore, the variational dynamic equations of the flexible system can be obtained as

$$\delta\boldsymbol{q}^{\mathrm{T}}(\boldsymbol{M}\ddot{\boldsymbol{q}}+\boldsymbol{Q}^{\infty}+\boldsymbol{Q}^{v}-\boldsymbol{Q}^{\mathrm{ext}}) = \boldsymbol{0} \tag{27}$$

## 3. Computational strategy

### 3.1. Dynamic equations

In this study, the electric field is applied by the preset charge loading, which means that the electric potential is known in advance. For constrained dynamic system, the constraint equations are presented as $\Phi = \mathbf{0}$ and $\Phi_{\boldsymbol{q}} = \partial\Phi/\partial\boldsymbol{q}$ is the Jacobian matrix. Introducing Lagrange multipliers $\boldsymbol{\lambda}$ to the constrained system, the dynamic equations are obtained

$$\overline{\Phi} = \begin{bmatrix} \boldsymbol{M}\ddot{\boldsymbol{q}} + \boldsymbol{Q}^d + \boldsymbol{Q}^\infty + \boldsymbol{Q}^e - \boldsymbol{Q}^{\text{ext}} + \Phi_{\boldsymbol{q}}^{\mathrm{T}}\boldsymbol{\lambda} \\ \Phi \end{bmatrix} = \mathbf{0} \tag{28}$$

where an additional generalized structural damping force $\boldsymbol{Q}^d = \boldsymbol{C}^d\dot{\boldsymbol{q}}$ is considered to reduce numerical oscillation of dynamic results. Taking the structural damping coefficient as $c_d$, the relationship between structural damping matrix and the mass matrix is expressed as $\boldsymbol{C}^d = c_d\boldsymbol{M}$.

To solve dynamic equations with the implicit time-integration algorithm, the Jacobian matrix of the system is needed

$$\overline{\boldsymbol{J}} = \begin{bmatrix} \boldsymbol{M}\dfrac{\partial\ddot{\boldsymbol{q}}}{\partial\boldsymbol{q}} + \boldsymbol{C}^d\dfrac{\partial\dot{\boldsymbol{q}}}{\partial\boldsymbol{q}} + \boldsymbol{J}^\infty + \boldsymbol{J}^e & \Phi_{\boldsymbol{q}}^{\mathrm{T}} \\ \Phi_{\boldsymbol{q}} & \mathbf{0} \end{bmatrix} \tag{29}$$

$$\boldsymbol{J}^\infty = \sum_{e=1}^{ne}\boldsymbol{B}_e^{\mathrm{T}}\boldsymbol{J}_e^\infty\boldsymbol{B}_e,\ \boldsymbol{J}^e = \sum_{e=1}^{ne}\sum_s\boldsymbol{B}_e^{\mathrm{T}}\left(\boldsymbol{J}_e^e\right)_s\boldsymbol{B}_e \tag{30}$$

where $\boldsymbol{J}^\infty$ and $\boldsymbol{J}^e$ are separately derived in Appendix 3.

### 3.2. Computational procedure

In this investigation, the dynamic results are obtained by solving the dynamic equations with the generalized-α method. To effectively filter out the high-frequency components of dynamic responses, the numerical damping of the generalized α method is considered in the computational procedure, which is controlled by the spectral radius $\rho_\infty = 0.8$. The parameters used in the generalized α method can be expressed by $\rho_\infty$ as

$$\alpha_m = \frac{2\rho_\infty - 1}{\rho_\infty + 1}, \alpha_f = \frac{\rho_\infty}{\rho_\infty + 1} \tag{31}$$

$$\gamma = 0.5 + \alpha_f - \alpha_m, \beta = 0.25(\gamma + 0.5)^2 \tag{32}$$

At the initial time, the time increment and the element coordinates are set as $\Delta t_0 = 10^{-4}s$ and $\boldsymbol{q}_e^0 = [\,(\boldsymbol{q}_e^{01})^{\mathrm{T}}\ \ (\boldsymbol{q}_e^{02})^{\mathrm{T}}\ \ \cdots\ \ (\boldsymbol{q}_e^{08})^{\mathrm{T}}\,]^{\mathrm{T}}$, respectively, where the initial nodal coordinates are given by $\boldsymbol{q}_e^{0i} = [\,(\boldsymbol{r}^{0i})^{\mathrm{T}}\ \ (\boldsymbol{r}_\xi^{0i})^{\mathrm{T}}\ \ (\boldsymbol{r}_\eta^{0i})^{\mathrm{T}}\ \ (\boldsymbol{r}_\zeta^{0i})^{\mathrm{T}}\,]^{\mathrm{T}}(i = 1, 2, \cdots, 8)$. The maximum and minimum value of the time increment $\Delta t_n$ are set as $(\Delta t_n)_{\max} = 10^{-4}s$ and $(\Delta t_n)_{\min} = 10^{-6}s$, respectively.

Let $n$ denote the number of time steps and $i$ denote the number of convergence cycles, the converged value $\boldsymbol{q}^{n+1}$, $\boldsymbol{\lambda}^{n+1}$ and $(\boldsymbol{C}_s^v)^{n+1}(s = 1, 2, \cdots, nv)$ at time $t_n$ ($t_n \leqslant t_{\text{total}}$) are calculated with the following steps, where $t_{\text{total}}$ is the total duration.

(1) Initialization

$$\begin{aligned} \boldsymbol{a}_0^{n+1} &= (\alpha_f\ddot{\boldsymbol{q}}^n - \alpha_m\boldsymbol{a}^n)/(1 - \alpha_m), \\ \boldsymbol{q}_0^{n+1} &= \boldsymbol{q}^n + \Delta t_n\dot{\boldsymbol{q}}^n + \Delta t_n^2(0.5 - \beta)\boldsymbol{a}^n + \Delta t_n^2\beta\boldsymbol{a}_0^{n+1}, \\ \dot{\boldsymbol{q}}_0^{n+1} &= \dot{\boldsymbol{q}}^n + \Delta t_n(1 - \gamma)\boldsymbol{a}^n + \Delta t_n\gamma\boldsymbol{a}_0^{n+1}, \\ \ddot{\boldsymbol{q}}_0^{n+1} &= \mathbf{0}, \boldsymbol{\lambda}_0^{n+1} = \mathbf{0}, (\boldsymbol{C}_s^v)_0^{n+1} = \boldsymbol{I}, \end{aligned} \tag{33}$$

where $\boldsymbol{a}$ is the acceleration vector and $\boldsymbol{I}$ is a three-dimensional unit matrix.

(2) Newton-Raphson iteration

$$\overline{\boldsymbol{J}}_i^{n+1}\begin{bmatrix} \Delta\boldsymbol{q}_i^{n+1} \\ \Delta\boldsymbol{\lambda}_i^{n+1} \end{bmatrix} = -\overline{\Phi}_i^{n+1} \tag{34}$$

where the increment of $\boldsymbol{q}_i^{n+1}$ and $\boldsymbol{\lambda}_i^{n+1}$ are both obtained as

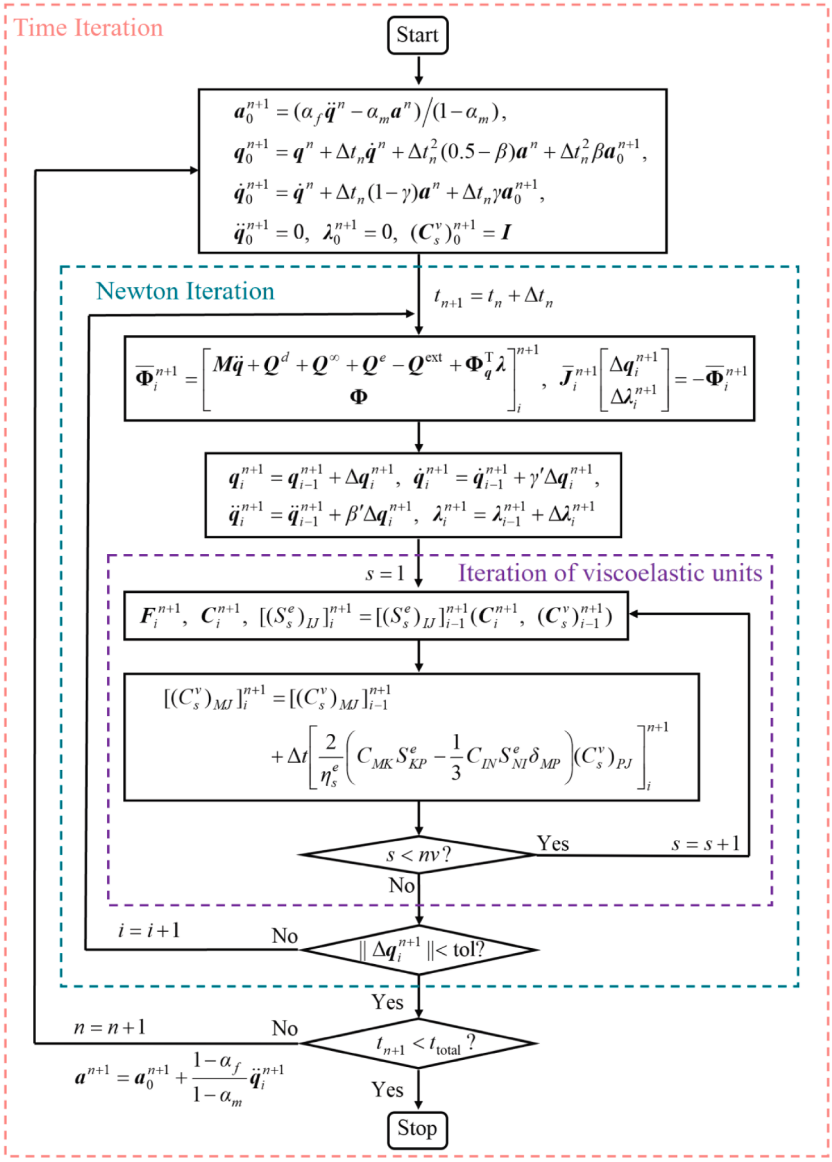


**Fig. 5.** Computational procedure of the generalized α method.

$$\begin{aligned} &\boldsymbol{q}_i^{n+1} = \boldsymbol{q}_{i-1}^{n+1} + \Delta \boldsymbol{q}_i^{n+1}, \dot{\boldsymbol{q}}_i^{n+1} = \dot{\boldsymbol{q}}_{i-1}^{n+1} + \gamma' \Delta \boldsymbol{q}_i^{n+1}, \\ &\ddot{\boldsymbol{q}}_i^{n+1} = \ddot{\boldsymbol{q}}_{i-1}^{n+1} + \beta' \Delta \boldsymbol{q}_i^{n+1}, \boldsymbol{\lambda}_i^{n+1} = \boldsymbol{\lambda}_{i-1}^{n+1} + \Delta \boldsymbol{\lambda}_i^{n+1}, \\ &\beta' = \frac{1-\alpha_m}{(1-\alpha_f)\beta \Delta t_n^2}, \gamma' = \frac{\gamma}{\beta \Delta t_n}. \end{aligned} \tag{35}$$

The deformation gradient $\boldsymbol{F}_i^{n+1}$ and the right Cauchy-Green tensor $\boldsymbol{C}_i^{n+1}$ are derived as

$$\boldsymbol{F}_i^{n+1} = \begin{bmatrix} \boldsymbol{S}_x & \boldsymbol{S}_y & \boldsymbol{S}_z \end{bmatrix}(\boldsymbol{q}_e)_i^{n+1}, \ \boldsymbol{C}_i^{n+1} = \left(\boldsymbol{F}_i^{n+1}\right)^{\mathrm{T}} \boldsymbol{F}_i^{n+1} \tag{36}$$

Subsequently, the viscous right Cauchy strain tensor $\boldsymbol{C}_s^v$ of viscoelastic unit $s$ is evolved by integrating the evolution equation using the Backward Euler method [38]

$$\begin{aligned} [(C_s^v)_{MJ}]_i^{n+1} = \Delta t\left[\frac{2}{\eta_s^e}\left(C_{MK}S_{KP}^e - \frac{1}{3}C_{IN}S_{NI}^e\delta_{MP}\right)(C_s^v)_{PJ}\right]_i^{n+1} \\ + [(C_s^v)_{MJ}]_{i-1}^{n+1} \end{aligned} \tag{37}$$

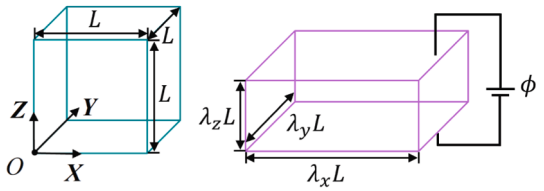


**Fig. 6.** Homogeneous deformation of a DE block. Reference configuration. (b) Current configuration.

$$[(S_s^e)_{IJ}]_i^{n+1} = \mu^e J^{e\,-2/3}[(R_s^e)_{IJ}^{-1}]_i^{n+1}[(C_s^v)_{IJ}^{-1}]_{i-1}^{n+1} - \frac{1}{3}\mu^e J^{e\,-2/3}[(R_s^e)_{IJ}^{-1}]_i^{n+1}(C_{QP}[(C_s^v)_{QP}^{-1}]C_{IJ}^{-1})_i^{n+1} + K^e(J^e-1)J^e(C_{IJ}^{-1})_i^{n+1}, \tag{38}$$

$$[(R_s^e)_{IJ}]_i^{n+1} = \left(1 - \frac{(J^{e\,-2/3}C_{QP}[(C_s^v)_{QP}^{-1}])_{i-1}^{n+1} - 3}{I_{\lim}^e}\right) \tag{39}$$

where $\eta_s^e$ is viscosity parameter of viscoelastic unit $s$.

Repeat (33) and (34) until $\|\Delta \boldsymbol{q}_i^{n+1}\|$ is less than the convergence precision tol $= 10^{-6}$ or the number of Newton-Raphson iteration $i$ reaches its limit.

(3) Update the acceleration at $t_{n+1}$ for the calculation of subsequent time steps

$$\boldsymbol{a}^{n+1} = \boldsymbol{a}_0^{n+1} + \frac{1-\alpha_f}{1-\alpha_m}\ddot{\boldsymbol{q}}_i^{n+1} \tag{40}$$

The detailed computational procedure is seen in Fig. 5. The viscous right Cauchy strain tensor of each viscoelastic unit is iterated individually. It should be noted that since electric potential is a predetermined input, the iterative calculation of $\varphi$ is not considered during the calculation.

## 4. Homogeneous deformation of a DE block

To demonstrate the capability of the proposed ANCF solid element for analyzing electrically-driven mechanics of DEAs, the homogeneous deformation of a DE block is simulated at first. As shown in Fig. 6(a), the DE block is in the shape of a cubic with side length $L$ in the reference configuration. To constrain the deformation to be homogeneous, boundary conditions of the cube are given as follows: $u_1 = 0$ on the $x = 0$ surface, $u_2 = 0$ on the $y = 0$ surface, $u_3 = 0$ on the $z = 0$ surface and $\varphi = 0$ on the $z = 0$ surface, where $u_1$, $u_2$ and $u_3$ are displacements along the inertial axis directions $\boldsymbol{X}$, $\boldsymbol{Y}$ and $\boldsymbol{Z}$, respectively. Subject to the loading voltage $\varphi$ in the $\boldsymbol{Z}$ direction, the cubic DE block deforms homogeneously and expands along both $\boldsymbol{X}$ and $\boldsymbol{Y}$ directions to the current configuration seen in Fig. 6(b). During the deforming process, principal stretches in the axis directions are expressed as $\lambda_x = \lambda_y$ and $\lambda_z = \lambda_x^{-2}$.

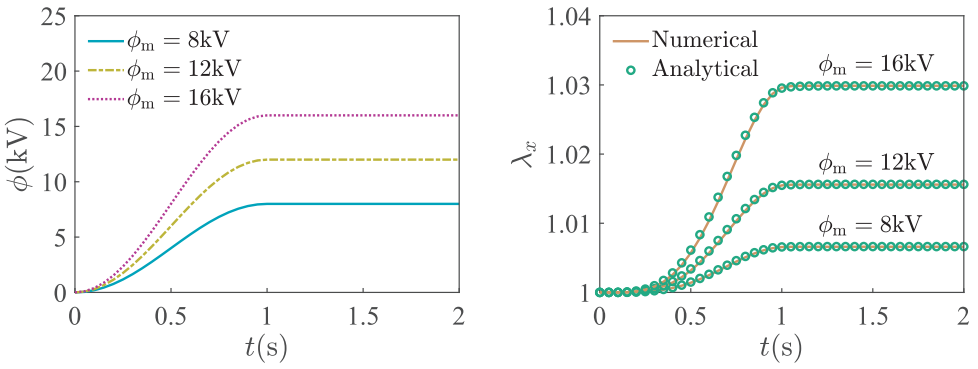


**Fig. 7.** Comparison of the analytical and numerical results. (a) The loading histories. (b) Lateral stretch as a function of time.

For the homogeneous deforming DE block, the viscoelastic model with one viscoelastic unit is adopted with $\mu^{\infty} = \mu_1^e = 67\text{kPa}$, $K^{\infty} = K_1^e = 6.7\text{GPa}$, $\eta_1^e = 3000$, $(I_{\text{lim}}^e)_1 = 5$ and $I_{\text{lim}}^{\infty} = 15$. The length, density and permittivity are given as $L = 1\text{mm}$, $\rho = 1.1\text{g/cm}^3$ and $\varepsilon = 4 \times 10^{-11}\text{F/m}$, respectively. In Appendix 4, the analytical solution is also provided as a reference.

On the surface of $z = L$, the applied voltage is set as

$$\varphi = \begin{cases} 0.5\varphi_{\text{m}}\sin(\pi t - 0.5\pi) + 0.5\varphi_{\text{m}} \\ \varphi_{\text{m}} \end{cases} \tag{41}$$

and three cases involving different charges are analyzed: $\varphi_{\text{m}} = 8\text{kV}$, $\varphi_{\text{m}} = 12\text{kV}$ and $\varphi_{\text{m}} = 16\text{kV}$, as seen in Fig. 7(a). It is observed in Fig. 7(b) that the increase of stretching ratio is obviously delayed compared with the loading of voltage because of the viscoelastic effect. Moreover, the simulated lateral stretches for the different values of $\varphi_{\text{m}}$ are in good agreement with the analytical results, which demonstrates the feasibility of the proposed viscoelastic model to predict the electrically-driven deformation of DEAs.

## 5. Inhomogeneous deformation of a torsional DEA

To demonstrate the feasibility of applying the proposed model to the DEAs with complex shapes that cannot be analytically addressed, the inhomogeneous deformation of a three-dimensional torsional DEA with one full twist over its length is further investigated. The length, width, and thickness are taken as $L_t = 60h_t$, $W_t = 10h_t$, and $h_t = 1\text{mm}$, respectively. Fig. 8(a) shows the undeformed discretized configuration of the torsional DEA, consisting of $ne = 768$ ANCF solid elements.

On the top surface, the applied voltage is given by $\varphi = \overline{\varphi} h_t (\varepsilon/\mu^{\infty})^{-0.5}$, where $\overline{\varphi}$ is the dimensionless electric potential. The final maximum value of the dimensionless normalized electric potential on the top surface is set as $\overline{\varphi}_m = 0.5$, while $\varphi$ is held at zero on the bottom surface. In Fig. 8(a), both ends of the actuator is constrained: the $x = 0$ surface is constrained to remain planar and not rotate, while the $x = L_t$ surface is only constrained to remain planar. Subject to the applied electric voltage, the torsional DEA shrinks in thickness, while expands in length and width, which make the front face rotate by an angle denoted by $\theta$, as seen in Fig. 8(b).

In the simulation, the density, permittivity, shear modulus, bulk modulus and limiting stretch parameter of the DEA are given as $\rho = 1.5\text{g/cm}^3$, $\varepsilon = 3.4 \times 10^{-11}\text{F/m}$, $\mu^{\infty} = 12\text{kPa}$, $K^{\infty} = 5\text{GPa}$ and $I_{\text{lim}}^{\infty} = 15$, respectively.

(b) Comparison between the predicted results with and without considering viscoelastic effect.

Without considering the viscoelastic effect, the actuation response $\theta$ is recorded as a function of dimensionless normalized electric potential $\overline{\varphi}$ in Fig. 9. As shown in Fig. 9(a), the predicted $\theta$ of the proposed dynamic model agrees well with the reference result from the previous research using the finite element formulation [44]. Compared with the finite element formulation, much fewer elements are used to guarantee the accuracy of the results by adopting the presented ANCF solid element, which improved the simulation efficiency.

Moreover, one can also investigate the viscoelastic effect of the torsional DEA by adopting the proposed viscoelastic model with one viscoelastic unit. Denoting the non-equilibrium shear modulus, bulk modulus, limiting stretch parameter and viscosity parameter as $\mu_1^e = 80\text{kPa}$, $K_s^e = 7.5\text{GPa}$, $(I_{\text{lim}}^e)_s = 5$ and $\eta_1^e = 400$, the predicted results with and without considering viscoelastic effect are compared in Fig. 9(b). Smaller twist angle is observed for the hyper-viscoelastic case, indicating the energy of the system is dissipated

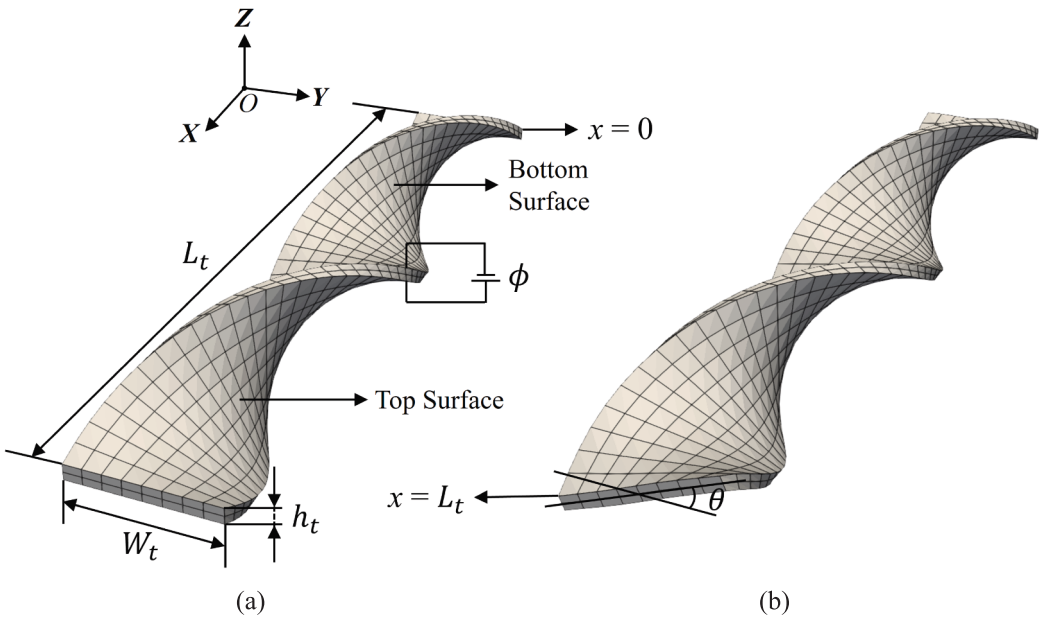


**Fig. 8.** Discretized configuration of the torsional DEA. (a) The reference configuration. (b) The current configuration.

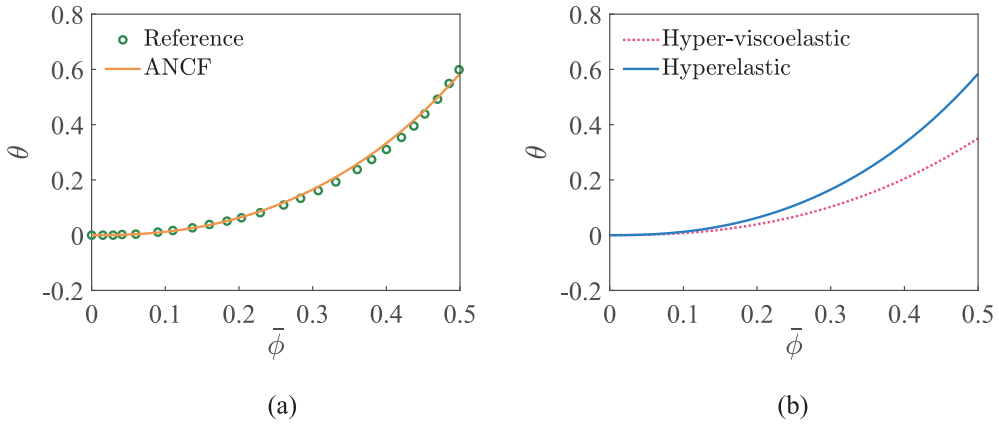


**Fig. 9.** Twist angle as a function of the dimensionless electric potential. (a) Comparison between the predicted results of the proposed model and the previous research.

due to the viscoelastic effect. This phenomenon reveals the importance of considering the viscoelastic effect, which will have a nonnegligible influence on the deforming performance of the DEAs.

## 6. Inhomogeneous deformation of a rolled DEA

The rolled DEAs can convert the biaxial stretching induced by an applied voltage into large uniaxial deformations, which has many potential applications and options for construction. In this section, a rolled DEA is designed and fabricated to validate the effectiveness of our dynamic model. The geometric dimensions of the rolled DEA are given as $h = 2$mm, $r = 2$mm and $L = 8$mm, as illustrated in Fig. 10.

### 6.1. Experiment setup

The rolled DEA is made of a customized dielectric elastomer that is produced by mixing two silicones (Sylgard 170 and Elastosil P7676) with improved electromechanical deformation capability and response speed [16]. To fabricate the rolled DEAs, it mainly involves following steps: i) The liquid silicone prepolymer solution is firstly mixed by a planetary stirrer (THINKY ARE 310, 5 min), which is composed of a mixture formulated with 90 % by mass of Elastosil P7676 (1:1 mix ratio) and 10 % by mass of Sylgard 170 (10:1 mix ratio); ii) the dielectric elastomer membrane (thickness of 35 um) is prepared by blade coating (Zehntner ZAA2300) onto a PET substrate and cured at 70℃ for 7 min; iii) the single wall carbon nanotube (SWCNT) based electrode is stamped onto the cured dielectric elastomer membrane; iv) a 7-layered dielectric elastomer membrane is obtained by repeating above process; v) The rolled DEA is fabricated by rolling the 7-layered dielectric elastomer membrane. The resultant DEA forms a hollow cylinder (inner diameter of 4 mm, outer diameters of 8 mm, and height of 8 mm). When a high voltage is applied, the rolled DEA can generate both axial and radial deformations. Especially, due to the radial limitation, the deformation is inhomogeneous, resulting in serious geometric nonlinearities.

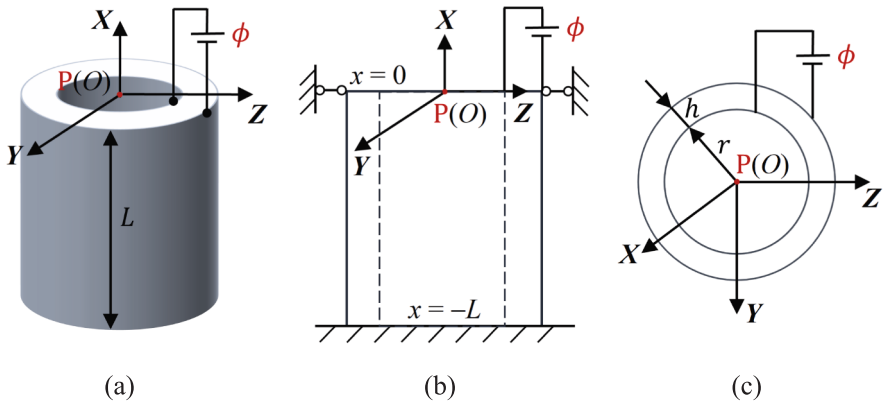


**Fig. 10.** Schematic diagram of a rolled DEA. (a) Perspective view. (b) Front view. (c) Top view.

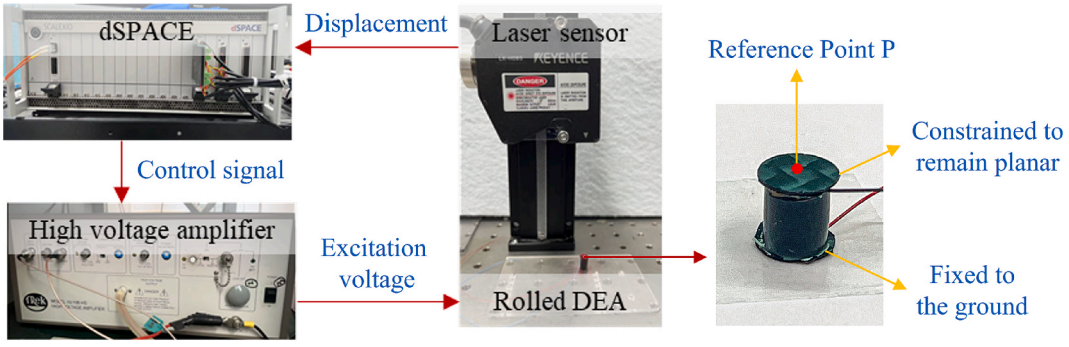


**Fig. 11.** Experimental setup.

To investigate the complex dynamic responses of the rolled DEA, we build an experimental setup, shown in Fig. 11. The experimental setup mainly consists of one high voltage amplifier (Trek 10/10B-HS), one laser sensors (Keyence LK-H085), and a control module (dSPACE Microlab 1202). The high voltage amplifier with a fixed gain of 1000 is adopted to provide excitation voltage. The laser sensor is used to measure the output displacement and convert it (in the range of −20 mm to 20 mm) into analog signal (in the range of −10 V to 10 V). The control module with 16-bit analog-to-digital (16-ADC) converter and 16-bit digital-to-analog converter (16-DAC) can generate control signal for the high voltage amplifier and record the displacement from the laser sensor (The sampling time is set as 1 ms in this work).

### 6.2. Experimental validation

Based on the experimental setup, dynamic responses of the rolled DEA are characterized by applying the sinusoidal loading voltage of

$$\varphi = 0.5\varphi_{\mathrm{m}}\sin(2\pi ft + 1.5\pi) + 0.5\varphi_{\mathrm{m}} \tag{42}$$

where the frequency and magnitude of the applied voltage are represented as $f$ and $\varphi_{\mathrm{m}}$, respectively. Hence, the duration of each cycle is obtained as $T = 1/f$. The displacement and velocity of the highest point P along the axis direction are expressed as $x$ and $\dot{x}$, respectively. In Fig. 10(b), both ends of the actuator are constrained: $u_2 = 0$ and $u_3 = 0$ on the top surface $x = 0$; $u_1 = 0$, $u_2 = 0$ and $u_3 = 0$ on the bottom surface $x = -L$, where $u_1$, $u_2$ and $u_3$ are displacements along the inertial axis directions $\boldsymbol{X}$, $\boldsymbol{Y}$ and $\boldsymbol{Z}$, respectively.

To study how the number of viscoelastic units affect the accuracy of the viscoelastic model, four different models are employed for dynamic simulations, including Model I with single viscoelastic unit, Model II with two viscoelastic units, Model III with three viscoelastic units and Model IV with four viscoelastic units, whose effectiveness will be examined through comparative experiments. In each the following simulations, the equilibrium bulk modulus and limiting stretch parameter are taken as $K^{\infty} = 3\mathrm{GPa}$ and $I_{\mathrm{lim}}^{\infty} = 15$, respectively. The non-equilibrium bulk modulus and limiting stretch parameter are kept unchanged as $K_s^e = 7.5\mathrm{GPa}$ and $(I_{\mathrm{lim}}^e)_s = 5$, while different values of $\mu^{\infty}$(kPa), $\mu_s^e$(kPa) and $\eta_s^e$ are taken as shown in Table 2 ($s = 1, 2, 3, 4$). The density and permittivity are given as $\rho = 1.5\mathrm{g/cm}^3$ and $\varepsilon = 3.4 \times 10^{-11}\mathrm{F/m}$, respectively.

The rolled DEA is modeled with $ne = n_l \times n_s \times n_r$ ANCF solid elements, where $n_l$, $n_s$ and $n_r$ are the number of elements along axial, circumferential and radial direction, respectively. By changing the element number in a single direction and keeping other directions constant, convergence of the predicted displacement at point P for given time ($t = 1/3s$) is investigated. The applied periodic voltage with ten cycles is shown in Fig. 12(a) where $f = 30\mathrm{Hz}$ and $\varphi_{\mathrm{m}} = 50\mathrm{kV}$.

According to Fig. 12(b), enough accuracy of the predicted results is achieved even when small number of elements are adopted in the axial and radial direction. However, the vertical displacement at point P cannot converge to a stable value until $n_s > 6$ in the circumferential direction. To ensure the accuracy and explicit more details of the deformed configuration, the rolled DEA is model with $ne = 12 \times 20 \times 4$ elements in the following simulations, as illustrated in Fig. 13.

Moreover, the predicted displacements of the rolled DEA at point P subject to the same loading voltage, as seen in Fig. 12(a), are also compared with the experimental results in Fig. 14.

**Table 2**
Material parameters of the rolled DEA.

| | $\mu^{\infty}$ | $\mu_1^e$ | $\mu_2^e$ | $\mu_3^e$ | $\mu_4^e$ | $\eta_1^e$ | $\eta_2^e$ | $\eta_3^e$ | $\eta_4^e$ |
|---|---|---|---|---|---|---|---|---|---|
| Model I | 81 | 80 | \ | \ | \ | 400 | \ | | \ |
| Model II | 78 | 30 | 80 | \ | \ | 300 | 200 | \ | \ |
| Model III | 75 | 10 | 40 | 80 | \ | 5000 | 300 | 100 | \ |
| Model IV | 72 | 10 | 10 | 80 | 80 | 5000 | 2000 | 300 | 100 |

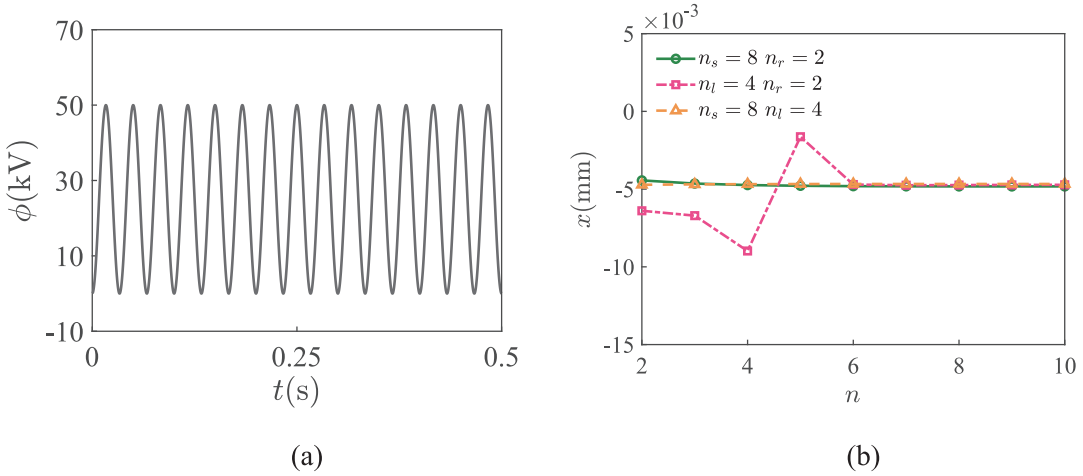


**Fig. 12.** Element convergence along axial, circumferential and radial direction. (a) The loading history. (b) The predicted displacement at point P for given time ($t = 1/3s$).

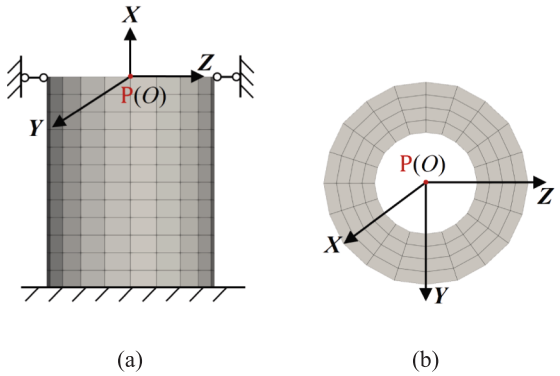


**Fig. 13.** The discretized elements of the rolled DEA. (a) Front view. (b) Top view.

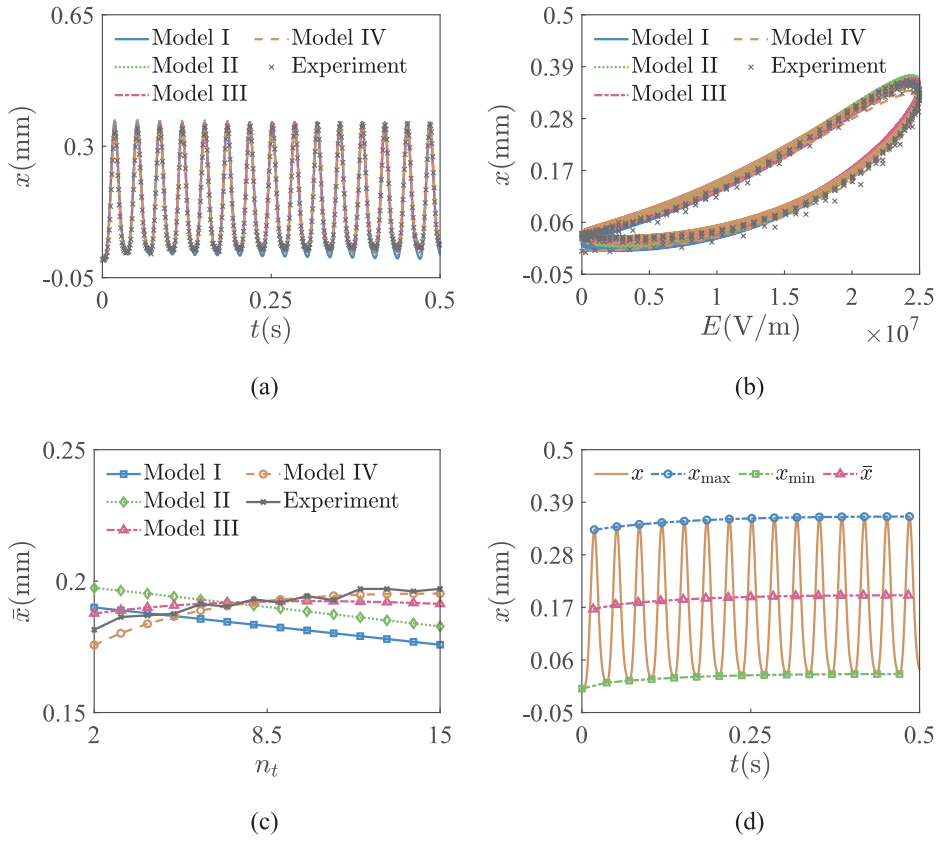


**Fig. 14.** Comparison of the numerical and experimental results of the rolled DEA subject to the cyclic voltage. (a) Displacement as a function of time. (b) Displacement as a function of electric field. (c) Average displacement of each cycle. (d) Maximum, minimum and average displacement of Model IV.

As shown in Fig. 14(a), the displacements at point P of all these models are drifting with time, which is generally explained as the viscoelastic creep. It is also noticed that the displacement in the loading process differs from the unloading results in each cycle, which leads to the hysteresis loop shown in Fig. 14(b). For each cycle, $x_{\max}$ and $x_{\min}$ are taken as the maximum displacement and minimum displacement at point P and the average displacement is given by $\bar{x} = 0.5(x_{\max} + x_{\min})$, as illustrated from the results of Model IV in Fig. 14(d). Considering the repeatable hysteresis loop can only be observed after the first cycle, taking the average displacement of the second cycle as $\bar{x}_0$, the direction of viscoelastic creep can be predicted through a creep parameter $k_c = \bar{x}/\bar{x}_0$. According to Fig. 14(c), the simulation results of Model IV creeps in the same direction as the experiment that the maximum and minimum displacements are both getting larger with time. However, the predicted results of Model I/II are simply drifting towards the opposite direction and the results of Model III only increase at first and then begin to decrease in the rest of time. Through the whole deforming process of the rolled DEA, the increasing differences between displacements of Model I/II/III and the experimental results are observed in Fig. 14(a). This phenomenon indicates that only the simulation results of Model IV can predict the experimental results properly, which addresses the necessity of increasing the number of viscoelastic units.

Adopting the same loading history in Eq. (42), a set of sinusoidal voltages are applied to the rolled DEA, with the magnitude of 25 kV and frequencies ranging from 10 Hz-70 Hz. To investigate the effect of changing frequency, it is assumed that the material parameters are kept constant when the frequency is different. The predicted axial displacement of the rolled DEA all agree well with the experiment in Fig. 15(a-h), which further verifies the feasibility of the proposed model under a wide range of frequencies. However, it is obvious that the area of the hysteresis loop increases as the frequency gets higher, as seen in Fig. 15(b, d, f, h), which indicates more viscoelastic effect of the DEA in the process of fast vibration.

Fig. 16(a, b) shows a detailed observation of the hysteresis loops for the last cycle, where the frequency increases from 10 Hz to 40 Hz and from 40 Hz to 70 Hz, respectively, which divides the changes in the hysteresis loop into two different stages. Mark two points in Fig. 16(a, b), including point A where $E = 0\text{V/m}$ and point B where $E = 2.5 \times 10^7\text{V/m}$. In the first stage, point B moves in the direction of decreasing displacement as the frequency increases from 10 Hz to 40 Hz, while point A remains in its original position, as shown in Fig. 16(a). However, in the second stage, the movement of point B is stopped as the frequency keeps increasing from 40 Hz, while point A begins to move along the direction of increasing displacement, as seen in Fig. 16(b). This phenomenon shows that employing the loading voltage with different frequencies will make the relationship between the displacement and electric field of the DEA change in stages.

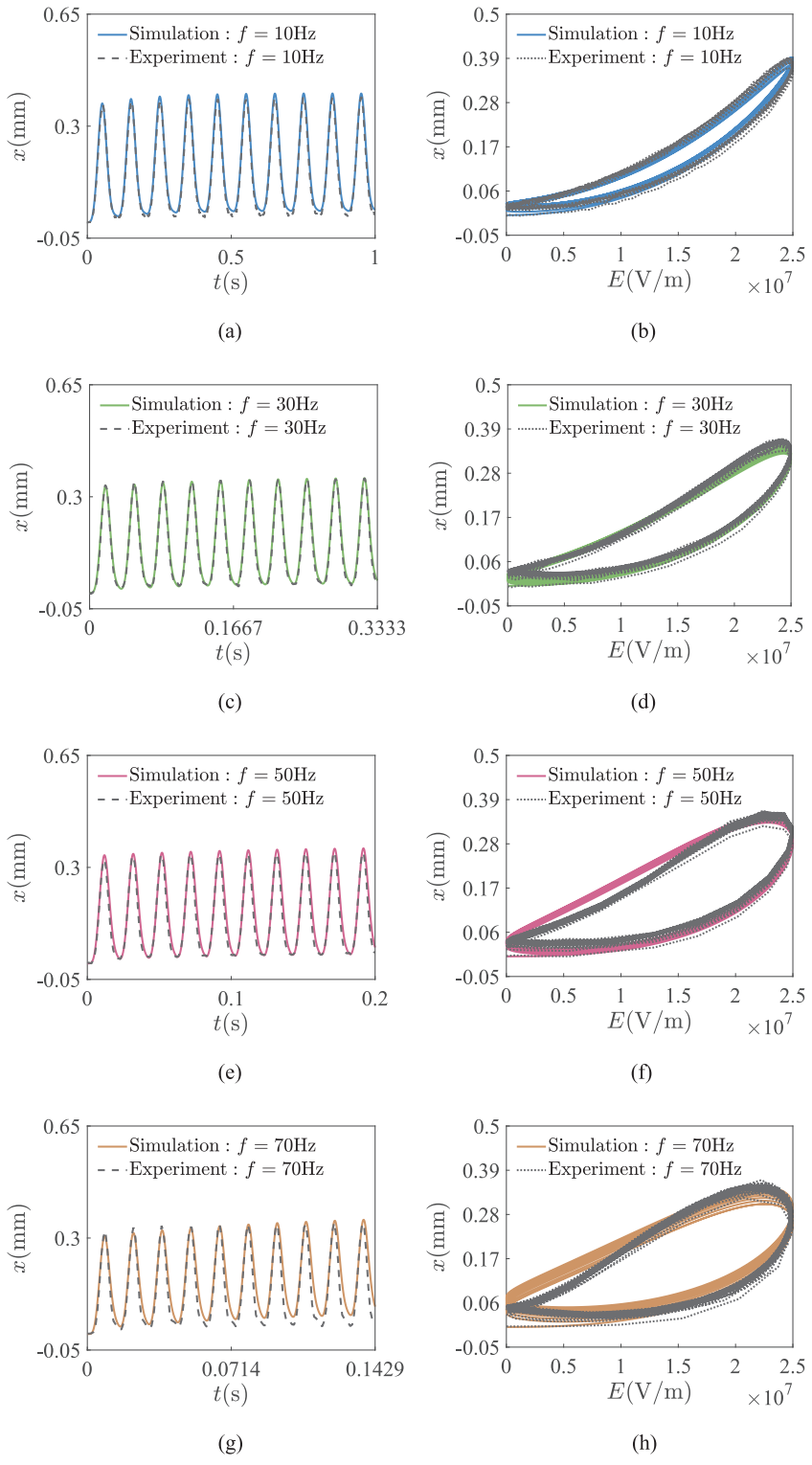


**Fig. 15.** The influence of the frequency of loading voltage on dynamic response of point P. (a, c, e, g) Displacement as a function of time. (b, d, f, h) Displacement as a function of electric field.

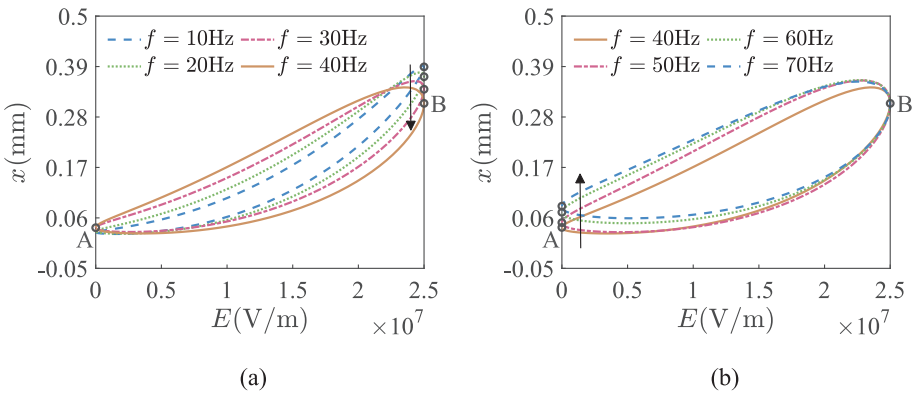


**Fig. 16.** Displacement at point P as a function of electric field for the last cycle. (a) Frequency increases from 10 Hz to 40 Hz. (b) Frequency increases from 40 Hz to 70 Hz.

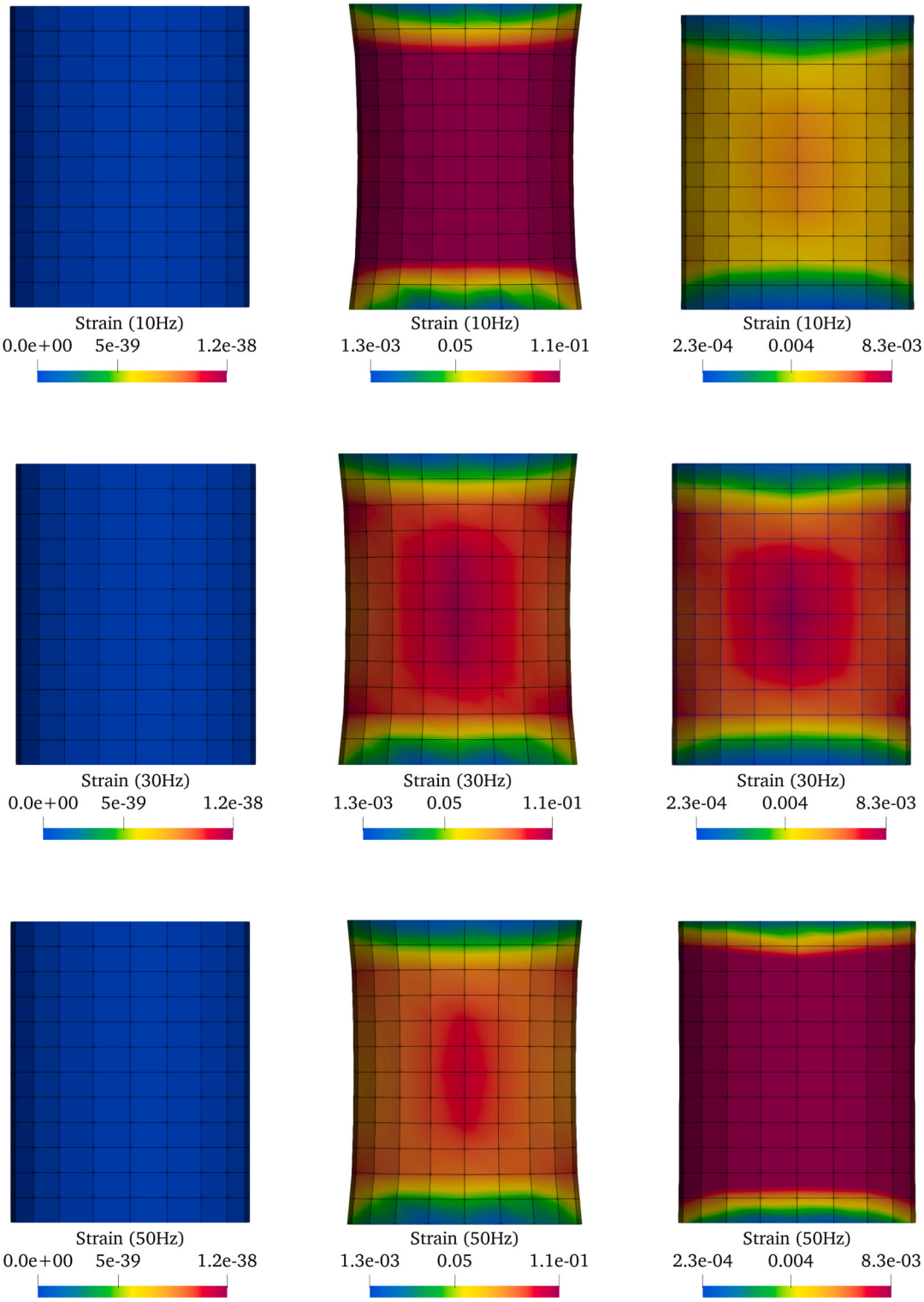


**Fig. 17.** Strain distribution of the rolled DEA through the first cycle with $f = 10, 30, 50, 70$ Hz. (a) From the front view at $t = 0$ s. (b) From the front view at $t = T/2$. (c) From the front view at $t = T$.

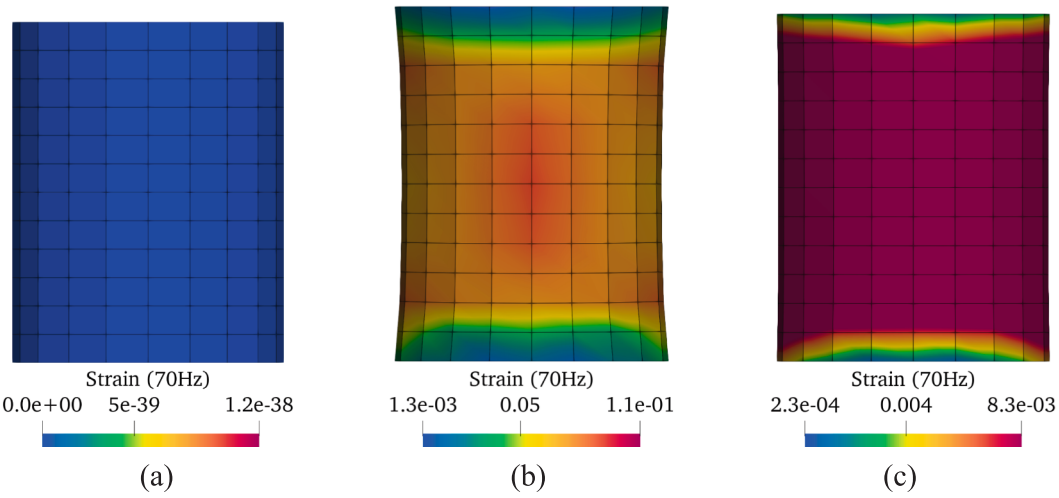


**Fig. 17.** (*continued*).

Strain distribution graph is used to illustrate the three-dimensional deformation of the rolled DEA. In Appendix 5, definition of the strain is presented. The strain distributions of the rolled DEA through the first cycle with different frequencies are shown in Fig. 17(a-c). Subject to the excitation voltage, the rolled DEA converts the biaxial expansion into the large deformation along the axial direction. Without support inside, large strain is exhibited at the waist position of the rolled DEA, as seen in Fig. 17(b). In case that $t = T/2$, the overall strain is smaller for the DEA with higher frequency, because more energy is dissipated by viscosity. However, in case that $t = T$, the strain residue after one deforming cycle is larger when higher frequency excitation is applied to the system, as shown in Fig. 17(c), due to the effect of more significant viscoelastic creep. The observed dynamic responses of the rolled DEA further reveal the geometric

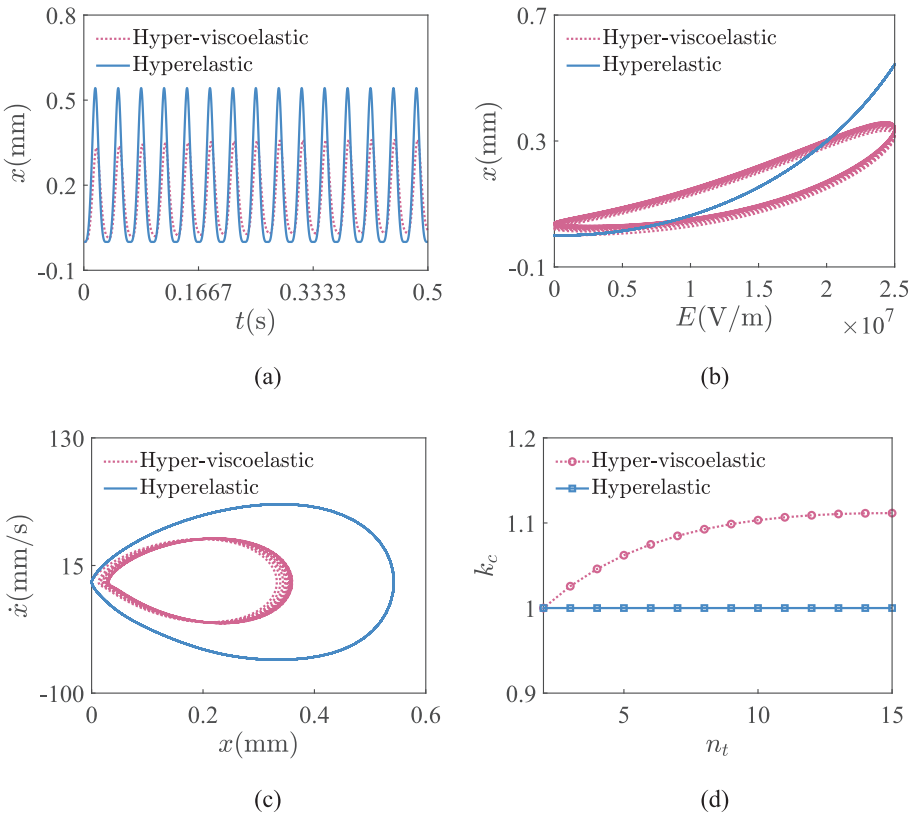


**Fig. 18.** Dynamic response of the rolled DEA at point P subject to the cyclic voltage. (a) Displacement as a function of time. (b) Displacement as a function of electric field. (c) Phase portrait. (d) Creep parameter in each cycle.

nonlinear characteristics and inhomogeneous deformation during the deforming process, emphasizing the importance of three-dimensional dynamic modeling.

### 6.3. *Effect of viscoelasticity*

To further illustrate the effect of considering viscoelasticity, the predicted hyper-viscoelastic results of Model IV are also compared with the hyperelastic case.

According to Fig. 18(a), smaller displacement is observed for the hyper-viscoelastic case because of the energy dissipation in the DEA subject to cyclic electrical loads. In Fig. 18(b, d), the DEA neither exhibits the repeatable hysteresis nor the viscoelastic creep when the viscoelasticity effect is not considered, which is quite different from the hyper-viscoelastic results. Fig. 18(c) depicts that the phase difference between velocity and displacement of point P is more significant for hyperelastic case, which is related to the viscoelastic effect as well. Besides, the closed loop of the hyperelastic case in Fig. 18(c) also suggests that deformation of the whole system is periodic without considering viscosity, which is not true for the hyper-viscoelastic case. Those differences between hyper-viscoelastic and hyperelastic cases reveal that the viscoelastic effect is non-negligible for investigating the vibration deformation of a DEA subject to periodic loading voltage.

For both of the hyper-viscoelastic and hyperelastic case, the strain distributions of the rolled DEA through the first cycle are illustrated in Fig. 19(a-c). Compared with the hyperelastic case, smaller strain is observed for the hyper-viscoelastic case at $t = T/2$, because the viscosity leads to the energy dissipation, as seen in Fig. 19(b). However, the strain residue of the hyper-viscoelastic case at $t = T$ is much larger than the hyperelastic case according to Fig. 19(c), since the system cannot return to the undeformed state after one deforming cycle due to the viscoelastic creep.

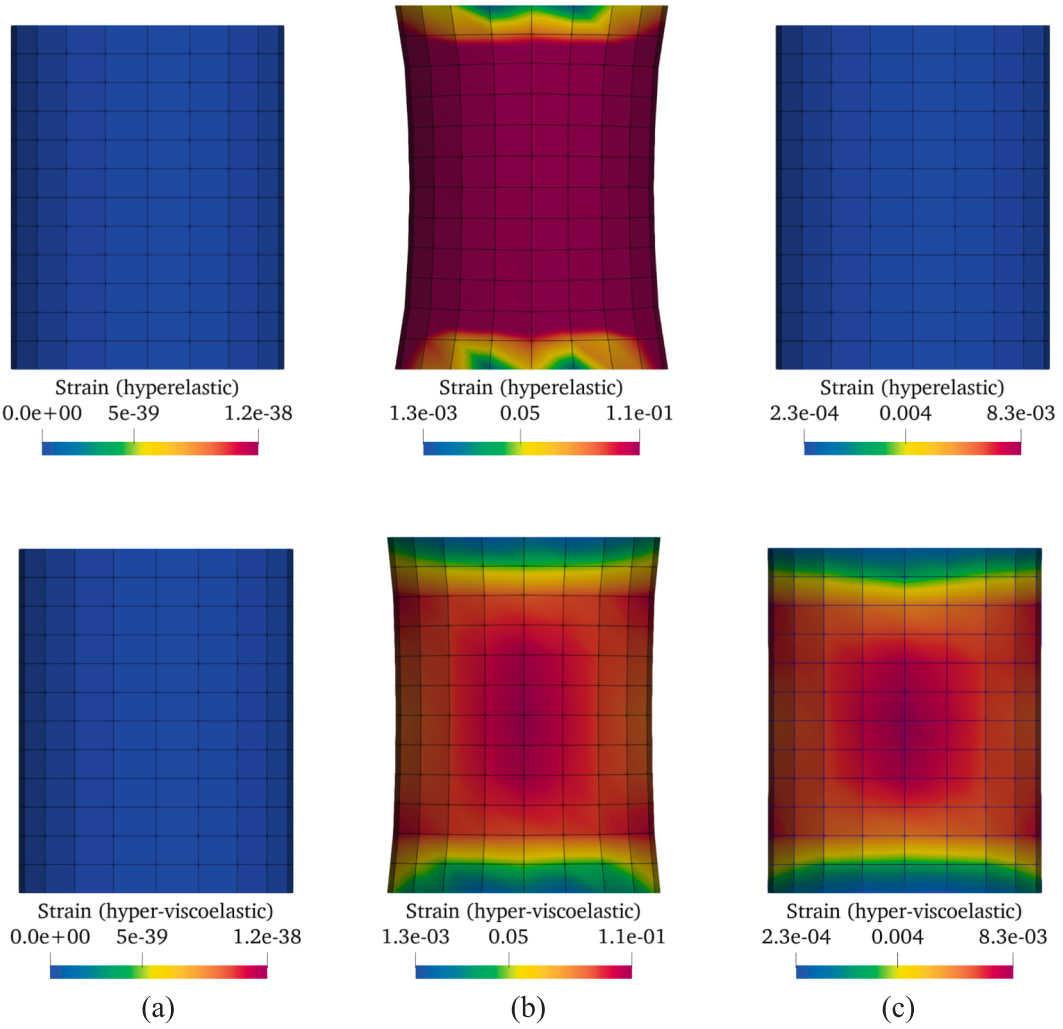


**Fig. 19.** Strain distribution of the rolled DEA for the hyper-viscoelastic and hyperelastic case. (a) From the front view at $t = 0$ s. (b) From the front view at $t = T/2$. (c) From the front view at $t = T$.

### 6.4. Effect of geometric parameters

To achieve good actuation properties of a rolled DEA, it is necessary to consider proper geometric parameters in the fabrication process, such as the thickness, the length and the cylindrical hollow volume at the center. Apparently, different geometric parameters will have different effects on the working performance of the actuator, meeting different needs for different situations.

Since the loading voltage is applied on the thickness $h$, its influence on the deformation and viscoelastic behavior of the rolled DEA is firstly investigated. For this purpose, a series of dynamic simulations are conducted by applying the loading voltage in Eq. (42) with $f = 30$Hz and set the magnitude of electric field intensity per unit thickness as $\varphi_m/h = 2.5 \times 10^7$V/m. Three different thickness are taken as $h = 2$mm, $h = 8$mm and $h = 14$mm, while other geometric parameters are kept unchanged. It can be seen in Fig. 20 (a, d) that as $h$ increases, smaller $\overline{x}_{\max}$ and constant $\overline{x}_{\min}$ are both observed, indicating smaller vibration amplitude for the whole system. It is also worth noting that the rolled DEA should be fabricated with $h$ no less than 1 mm, since a local minimum of the displacement $x$ occurs at $h \in (0, 1]$, which means larger deformation is no longer guaranteed by overcoming the difficulties of reducing $h$ in the fabrication process. Furthermore, more significant amount of hysteresis and faster creep speed are also observed in Fig. 20(b, c) when smaller $h$ is achieved, exhibiting more obvious viscoelastic effect of the rolled DEA.

Considering the rolled DEA mainly deforms in the length direction, the influence of changing the length of the whole actuator on its deforming performance is also analyzed in this section. By applying the loading voltage in Eq. (42) with $f = 30$Hz and $\varphi_m = 50$kV, three different cases are analyzed: $L = 10$mm, $L = 38$mm and $L = 66$mm. Contrary to the changes caused by increasing thickness, larger $L$ leads to greater deformation, more hysteresis and larger $\overline{x}_{\max}$ for the DEA, as seen in Fig. 21(a, b, d). In Fig. 21(d), $\overline{x}_{\max}$ increases linearly and monotonically with the increase of $L$, while $\overline{x}_{\min}$ keeps unchanged first and then decreases to a negative value as $L > 54$ mm, which means that the DEA is no longer elongated in the length direction, but shortened when $x = x_{\min}$. This phenomenon probably results from the changes in the natural frequency of the rolled DEA when $L$ is extremely large, which also makes the shape of the hysteresis loop change from a single ring into a couple rings for the case of $L = 66$ mm in Fig. 21(b). Meanwhile, increasing $L$ also slows down the creep speed of the displacement, as shown in Fig. 21 (c), which is similar to the effect of increasing $h$ in Fig. 20(d).

At the center of the rolled DEA, the cylindrical hollow volume can be characterized by the radius $r$ of the cross section, whose influence on the displacement $x$ is studied next. By adopting the loading voltage in Eq. (42) with $f = 30$Hz and $\varphi_m = 50$kV, the investigations involving three different radius are conducted: $r = 0$mm, $r = 28$mm and $r = 56$mm. According to Fig. 22(d), increasing $r$ achieves smaller $\overline{x}_{\max}$ when $r \leqslant 16$ mm, but has little influence on $\overline{x}_{\min}$ at the same time. However, as $r$ continues to increase from 16 mm, there will be no more significant changes in both $\overline{x}_{\max}$ and $\overline{x}_{\min}$. Additionally, less viscoelastic effect of the DEA is exhibited with

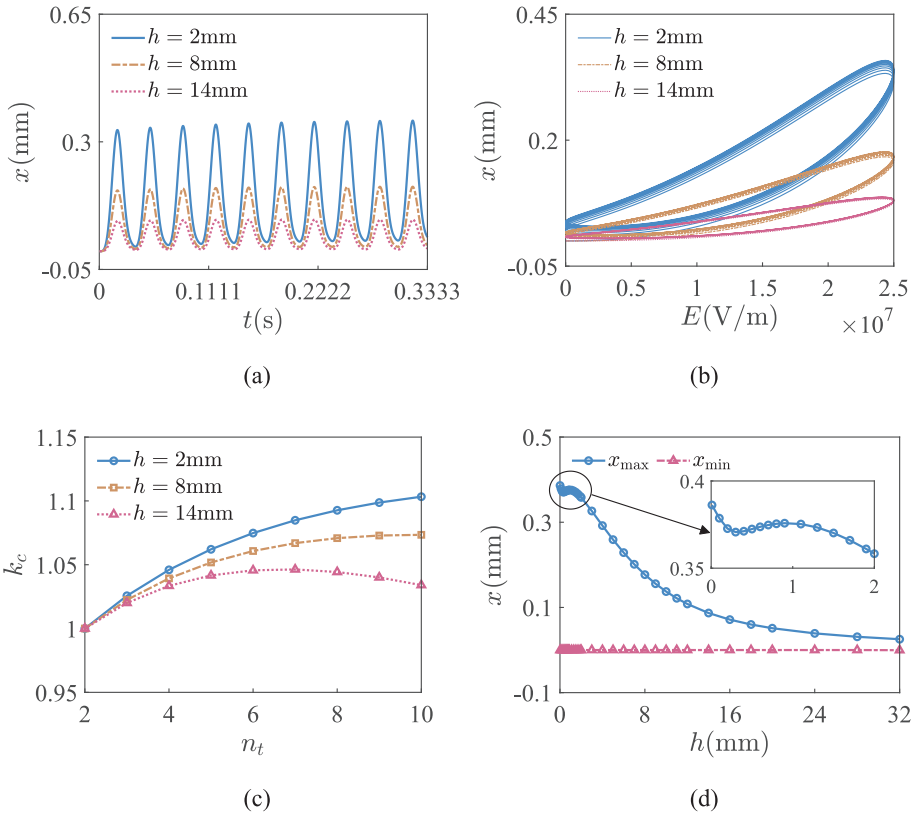


**Fig. 20.** The influence of thickness on dynamic response of point P. (a) Displacement as a function of time. (b) Displacement as a function of electric field. (c) Creep parameter as a function of time after the second cycle. (d) Maximum and minimum displacement in each cycle.

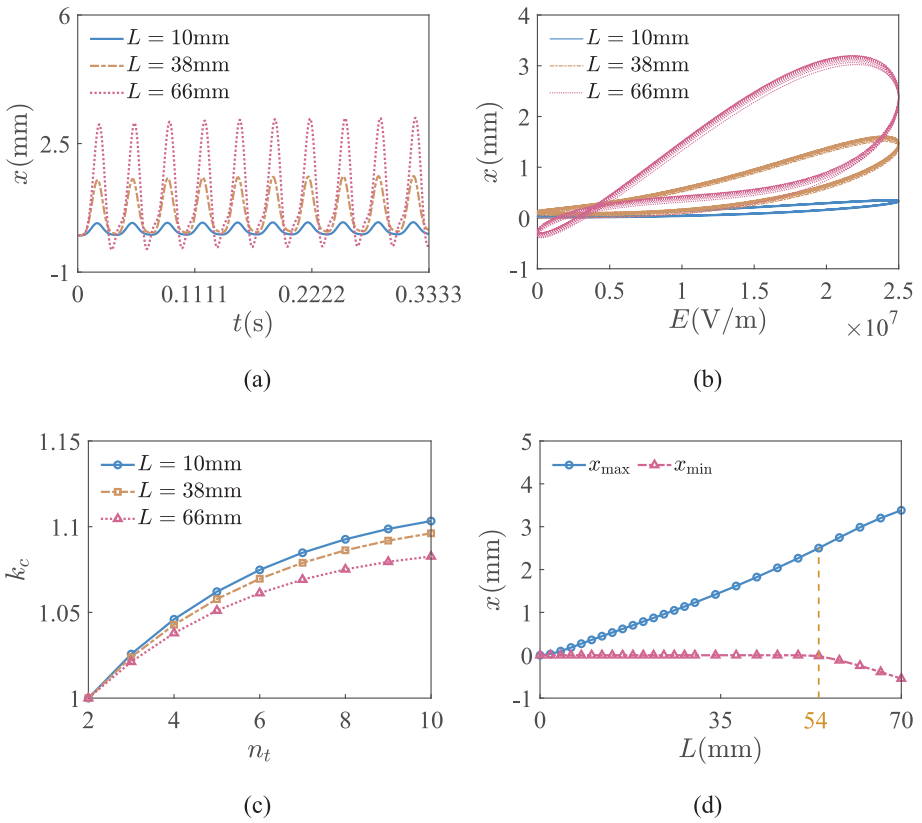


**Fig. 21.** The influence of length on dynamic response of point P. (a) Displacement as a function of time. (b) Displacement as a function of electric field. (c) Creep parameter as a function of time after the second cycle. (d) Maximum and minimum displacement in each cycle.

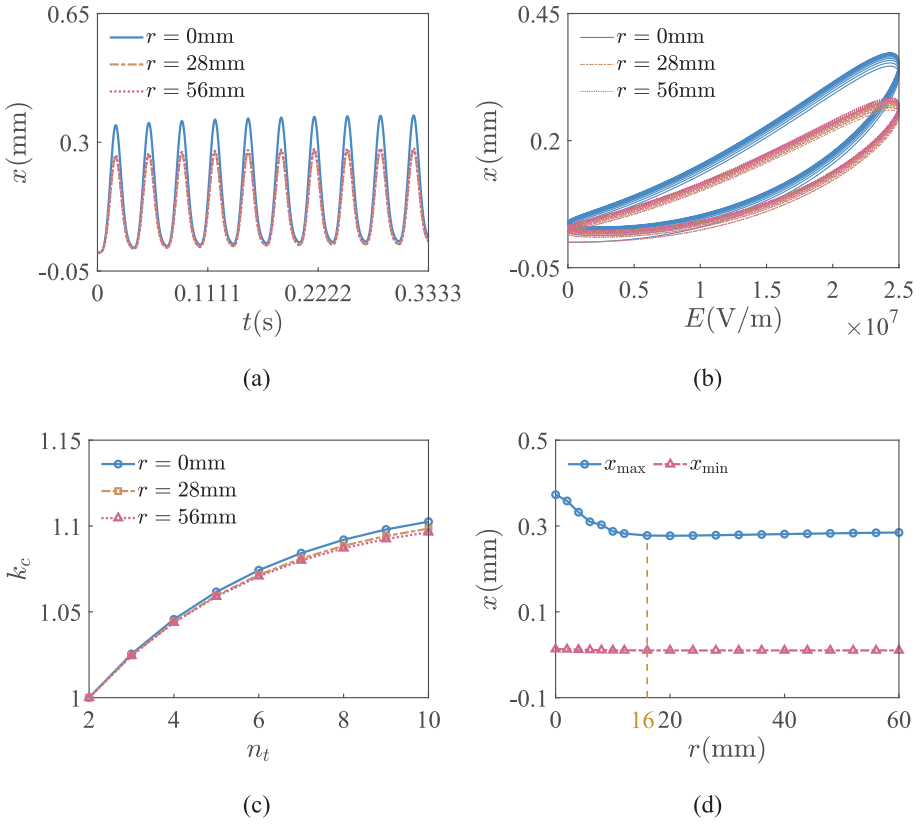


**Fig. 22.** The influence of radius on dynamic response of point P. (a) Displacement as a function of time. (b) Displacement as a function of electric field. (c) Creep parameter as a function of time after the second cycle. (d) Maximum and minimum displacement in each cycle.

the increase of $r$ for the case that $r \leqslant 16$ mm, since smaller hysteresis loop and slower creep speed are both observed in Fig. 22(b, c). Although different radius will have certain influence on the actuation properties of the rolled DEA, its influence is worth considering only when $r \leqslant 16$ mm.

### 6.5. *Effect of different loading voltages*

To provide references for controlling a rolled DEA, this subsection analyzes its dynamic responses subject to different loading voltages through more numerical cases.

Subject to the loading voltages in Eq. (42) with a constant frequency $f = 30$Hz and different magnitudes, the viscoelastic behaviors of the rolled DEA are further predicted for three different cases: $\varphi_{\mathrm{m}} = 6$kV, $\varphi_{\mathrm{m}} = 8$kV and $\varphi_{\mathrm{m}} = 10$kV. Fig. 23(b) shows that the deformation is increased with larger $\varphi_{\mathrm{m}}$, which is because of the increased attraction between opposite charges on the electrodes. As depicted in Fig. 23(c), all the three hysteresis loops are in the same shape of different sizes, where larger hysteresis loop means more significant viscoelastic effect. However, taking different $\varphi_{\mathrm{m}}$ only has slight influence on the viscoelastic creep of the DEA, according to the coincident curves in Fig. 23(d).

Furthermore, the influence of the voltage patterns with different loading histories on the actuation properties of the rolled DEA are also studied. Two different loading voltages are applied as shown in Fig. 24(a, b), which are named as VP1 and VP2 from left to right. Through dynamic simulations, some notable phenomena of the DEA can be observed in the hysteresis loops in Fig. 24(c, d), such as the memory effects, wiping-out and congruency properties [39]. As seen in Fig. 24(c), the hysteresis shows the memory effects with both the major loop and the minor loop, depending upon the loading histories with different amplitudes. In addition, the wiping-out property is also exhibited that the hysteresis output depends upon not only the current input but also the previous dominant input extrema. In Fig. 24(d), two minor hysteresis loops corresponding to the same input range are congruent inside the major loop, which reveals the congruency property of the DEA as well. These cases with different voltage patterns further illustrate the ability of the proposed model to describe the unique material properties of DEAs.

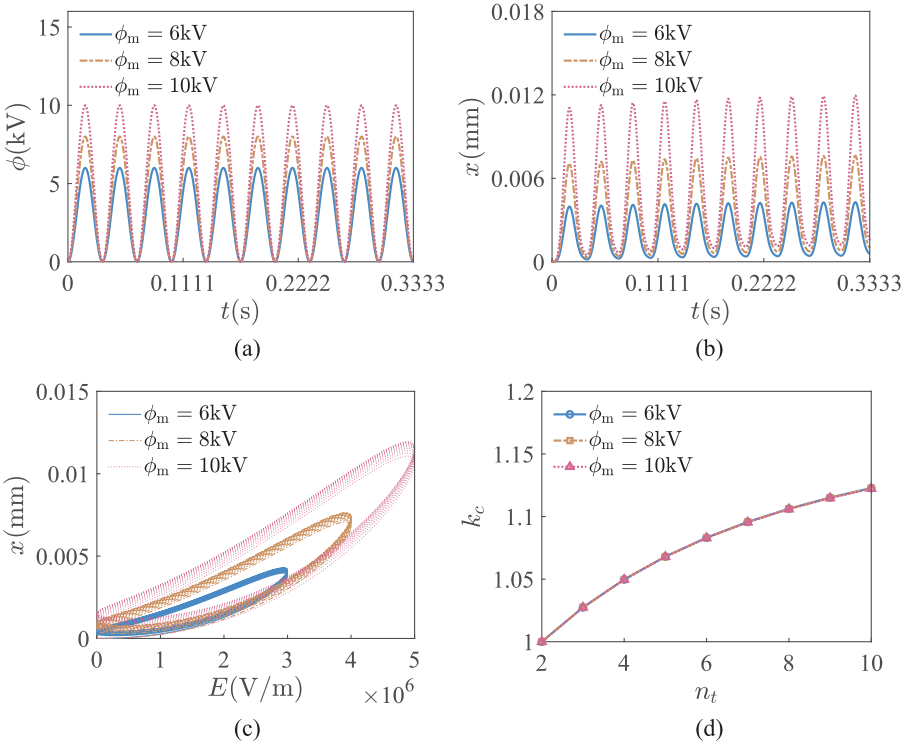


**Fig. 23.** The influence of $\varphi_m$ on dynamic response of point P. (a) The loading history. (b) Displacement as a function of time. (c) Displacement as a function of electric field. (d) Creep parameter as a function of time after the second cycle.

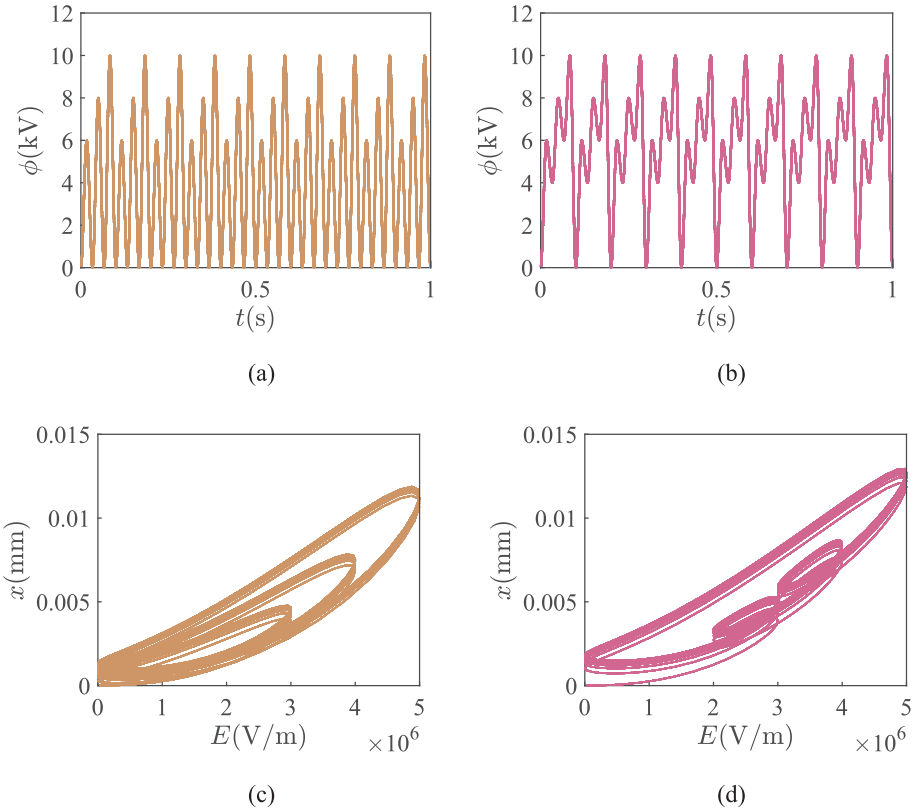


**Fig. 24.** Dynamic response of point P subject to ten cycles of different voltage patterns. (a, b) The loading history. (c, d) Displacement as a function of time.

## 7. Conclusions

In this paper, a numerical framework for dynamic modeling of arbitrary shaped DEAs is proposed, considering both geometric nonlinearity and viscoelasticity. Different from conventional viscoelastic models, the proposed model combines the ANCF method with a viscoelastic model adopting multiple viscoelastic units, such that it can be used for modeling of DEAs with complex shapes subject to cyclic loading voltages. The absolute nodal position vectors and their gradients with respect to material coordinates are used as generalized coordinates, which can describe the rigid-body motions and large deformations for arbitrary shaped DEAs. The volumetric locking of incompressible material is effectively avoided by using high-order interpolation functions. Subsequently, the generalized force vectors and their Jacobians are deduced as well as the mass matrix of the whole system. According to Hamilton's principle, dynamic equations of the flexible system are derived, which are solved by applying the generalized α method.

Firstly, the homogeneous deformations of a DE block are predicted with the proposed model and the numerical results agree well with the analytical solutions. Secondly, the proposed model is proved to be applicable to the DEAs with complex shapes by investigating the dynamic performance of a three-dimensional torsional DEA. Next, the effectiveness of the proposed model under a wide frequency range is verified by conducting experiments and dynamic simulations on a rolled DEA with inhomogeneous 3D deformations. By increasing the number of viscoelastic units in the viscoelastic model from one to four, good agreement between the predicted results and the experimental results is achieved. Subsequently, the necessity of considering viscoelastic effect is further demonstrated through the unique phenomena that are unobservable in the hyper-elastic cases, including the aperiodic deformations, hysteresis phenomenon, and additional energy dissipation.

Finally, the influence of geometric parameters and different loading voltages on the actuation performances of the rolled DEA is investigated. According to the results, good actuation properties with large axis displacement and less viscoelastic effect can be achieved by fabricating the rolled DEA with appropriate geometric parameters. In addition, more notable properties such as the wiping-out property, the congruency property and the memory effects are also observed by applying different loading histories to the rolled DEA. The proposed viscoelastic dynamic model will provide further references for the future analysis of the viscoelastic behaviors in the DEAs with different shapes.

## 8. Code availability

The custom codes cannot be shared for this time as they are related to another ongoing study.

### CRediT authorship contribution statement

**Liwen Zhang:** Writing – original draft. **Xiaotian Shi:** Validation. **Guoying Gu:** Writing – review & editing. **Jiang Zou:** Writing – review & editing. **Jinyang Liu:** Writing – review & editing.

### Declaration of competing interest

The authors declare that they have no known competing financial interests or personal relationships that could have appeared to influence the work reported in this paper.

### Acknowledgements

This research was supported by the General Program (No. 12272221) of the National Natural Science Foundation of China, the International (Regional) Cooperation and Exchange Programs (No. 12311530038) of the National Natural Science Foundation of China, the National Natural Science Foundation of China (No. 52275024), and the Natural Science Foundation of Shanghai (No. 24511103602), for which the authors are grateful.

### Appendix 1

In the following, the detailed components of the shape function in the material coordinate system are presented as

$$\begin{aligned} s_{i1} &= \frac{1}{16}(1+\xi_i\xi)(1+\eta_i\eta)(1+\zeta_i\zeta)f_i, \\ s_{i2} &= \frac{a}{32}\xi_i(1+\xi_i\xi)(1+\eta_i\eta)(1+\zeta_i\zeta)(\xi_i^2\xi^2-1), \\ s_{i3} &= \frac{b}{32}\eta_i(1+\xi_i\xi)(1+\eta_i\eta)(1+\zeta_i\zeta)(\eta_i^2\eta^2-1), \\ s_{i4} &= \frac{c}{32}\zeta_i(1+\xi_i\xi)(1+\eta_i\eta)(1+\zeta_i\zeta)(\zeta_i^2\zeta^2-1), \\ f_i &= (2+\xi_i\xi+\eta_i\eta+\zeta_i\zeta-\xi_i^2\xi^2-\eta_i^2\eta^2-\zeta_i^2\zeta^2), \end{aligned} \tag{43}$$

where $(\xi_i,\eta_i,\zeta_i)$ is the local material coordinates of node $i$ ($i=1,2,\cdots,8$). Each one of $\xi_i$, $\eta_i$ and $\zeta_i$ is either $-1$ or 1 depending on the

specific location of the node.

The partial derivatives of shape function components along axis $\boldsymbol{\xi}$ are written as

$$\begin{aligned}
(s_{i1})_{\xi} &= \frac{1}{16}(1+\eta_i\eta)(1+\zeta_i\zeta)[\xi_i f_i + (1+\xi_i\xi)(f_i)_{\xi}],\\
(s_{i2})_{\xi} &= \frac{1}{16}(1+\eta_i\eta)(1+\zeta_i\zeta)\xi_i[\xi_i(\xi_i^2\xi^2-1)]\\
&+\frac{1}{16}(1+\eta_i\eta)(1+\zeta_i\zeta)\xi_i[(1+\xi_i\xi)(2\xi_i^2\xi)],\\
(s_{i3})_{\xi} &= \frac{1}{16}\eta_i\xi_i(1+\eta_i\eta)(1+\zeta_i\zeta)(\eta_i^2\eta^2-1),\\
(s_{i4})_{\xi} &= \frac{1}{16}\zeta_i\xi_i(1+\eta_i\eta)(1+\zeta_i\zeta)(\zeta_i^2\zeta^2-1),\\
(f_i)_{\xi} &= (\xi_i - 2\xi_i^2\xi).
\end{aligned} \tag{44}$$

The partial derivatives of shape function components along axis $\boldsymbol{\eta}$ can also be derived as

$$\begin{aligned}
(s_{i1})_{\eta} &= \frac{1}{16}(1+\xi_i\xi)(1+\zeta_i\zeta)[\eta_i f_i + (1+\eta_i\eta)(f_i)_{\eta}],\\
(s_{i2})_{\eta} &= \frac{1}{16}\xi_i\eta_i(1+\xi_i\xi)(1+\zeta_i\zeta)(\xi_i^2\xi^2-1),\\
(s_{i3})_{\eta} &= \frac{1}{16}(1+\xi_i\xi)(1+\zeta_i\zeta)\eta_i[\eta_i(\eta_i^2\eta^2-1)]\\
&+\frac{1}{16}(1+\xi_i\xi)(1+\zeta_i\zeta)\eta_i[(1+\eta_i\eta)(2\eta_i^2\eta)],\\
(s_{i4})_{\eta} &= \frac{1}{16}\zeta_i\eta_i(1+\xi_i\xi)(1+\zeta_i\zeta)(\zeta_i^2\zeta^2-1),\\
(f_i)_{\eta} &= (\eta_i - 2\eta_i^2\eta).
\end{aligned} \tag{45}$$

The partial derivatives of shape function components along axis $\boldsymbol{\zeta}$ are expressed as

$$\begin{aligned}
(s_{i1})_{\zeta} &= \frac{1}{16}(1+\xi_i\xi)(1+\eta_i\eta)[\zeta_i f_i + (1+\zeta_i\zeta)(f_i)_{\zeta}],\\
(s_{i2})_{\zeta} &= \frac{1}{16}\xi_i\zeta_i(1+\xi_i\xi)(1+\eta_i\eta)(\zeta_i^2\zeta^2-1),\\
(s_{i3})_{\zeta} &= \frac{1}{16}\eta_i\zeta_i(1+\xi_i\xi)(1+\eta_i\eta)(\eta_i^2\eta^2-1),\\
(s_{i4})_{\zeta} &= \frac{1}{16}(1+\xi_i\xi)(1+\eta_i\eta)\zeta_i[\zeta_i(\zeta_i^2\zeta^2-1)]\\
&+\frac{1}{16}(1+\xi_i\xi)(1+\eta_i\eta)\zeta_i[(1+\zeta_i\zeta)(2\zeta_i^2\zeta)],\\
(f_i)_{\zeta} &= (\zeta_i - 2\zeta_i^2\zeta).
\end{aligned} \tag{46}$$

## Appendix 2

The derivation of trace of the elastic components of the right Cauchy strain tensor is given in appendix 2. According to Eq. (14), the elastic components of the right Cauchy strain tensor can be written as $\boldsymbol{C}^e = (\boldsymbol{F}^v)^{-\mathrm{T}}\boldsymbol{C}(\boldsymbol{F}^v)^{-1}$. Defining $\boldsymbol{C}^e = [C^e_{IJ}]$, $\boldsymbol{C} = [C_{IJ}]$, $\boldsymbol{F}^v = [F^v_{IJ}]$ and the viscous right Cauchy strain tensor as $\boldsymbol{C}^v = (\boldsymbol{F}^v)^{\mathrm{T}}\boldsymbol{F}^v$, each element of $\boldsymbol{C}^e$ can expressed as

$$C^e_{IJ} = \sum_{K=1}^{n}\sum_{P=1}^{n}(F^v_{KI})^{-1}C_{KP}(F^v_{PJ})^{-1} \tag{47}$$

The trace of $\boldsymbol{C}^e$ can be further obtained as

$$
\begin{aligned}
I_1^e &= \mathrm{tr}(C^e) = C_{II}^e = (F_{KI}^v)^{-1} C_{KP} (F_{PI}^v)^{-1} \\
&= C_{KP}((F_{KI}^v)^{-1}(F_{PI}^v)^{-1}) \\
&= C_{KP}((F_{KI}^v)^{-1}(F_{IP}^v)^{-\mathrm{T}}) = C_{KP}(C_{KP}^v)^{-1} \\
&= (C_{11}^v)^{-1} C_{11} + (C_{21}^v)^{-1} C_{21} + (C_{31}^v)^{-1} C_{31} \\
&+ (C_{12}^v)^{-1} C_{12} + (C_{22}^v)^{-1} C_{22} + (C_{32}^v)^{-1} C_{32} \\
&+ (C_{13}^v)^{-1} C_{13} + (C_{23}^v)^{-1} C_{23} + (C_{33}^v)^{-1} C_{33} \\
&= (C_{11}^v)^{-1} \boldsymbol{q}_e^{\mathrm{T}} \boldsymbol{S}_x^{\mathrm{T}} \boldsymbol{S}_x \boldsymbol{q}_e + (C_{21}^v)^{-1} \boldsymbol{q}_e^{\mathrm{T}} \boldsymbol{S}_x^{\mathrm{T}} \boldsymbol{S}_y \boldsymbol{q}_e \\
&+ (C_{31}^v)^{-1} \boldsymbol{q}_e^{\mathrm{T}} \boldsymbol{S}_x^{\mathrm{T}} \boldsymbol{S}_z \boldsymbol{q}_e + (C_{12}^v)^{-1} \boldsymbol{q}_e^{\mathrm{T}} \boldsymbol{S}_y^{\mathrm{T}} \boldsymbol{S}_x \boldsymbol{q}_e \\
&+ (C_{22}^v)^{-1} \boldsymbol{q}_e^{\mathrm{T}} \boldsymbol{S}_y^{\mathrm{T}} \boldsymbol{S}_y \boldsymbol{q}_e + (C_{32}^v)^{-1} \boldsymbol{q}_e^{\mathrm{T}} \boldsymbol{S}_y^{\mathrm{T}} \boldsymbol{S}_z \boldsymbol{q}_e \\
&+ (C_{13}^v)^{-1} \boldsymbol{q}_e^{\mathrm{T}} \boldsymbol{S}_z^{\mathrm{T}} \boldsymbol{S}_x \boldsymbol{q}_e + (C_{23}^v)^{-1} \boldsymbol{q}_e^{\mathrm{T}} \boldsymbol{S}_z^{\mathrm{T}} \boldsymbol{S}_y \boldsymbol{q}_e \\
&+ (C_{33}^v)^{-1} \boldsymbol{q}_e^{\mathrm{T}} \boldsymbol{S}_z^{\mathrm{T}} \boldsymbol{S}_z \boldsymbol{q}_e.
\end{aligned} \tag{48}
$$

Additionally, the above expression can also be simplified to the form of $I_1^e = \boldsymbol{q}_e^{\mathrm{T}} \boldsymbol{B} \boldsymbol{q}_e$, where

$$
\begin{aligned}
\boldsymbol{B} &= C_{11}^{v-1} \boldsymbol{S}_x^{\mathrm{T}} \boldsymbol{S}_x + C_{12}^{v-1} \boldsymbol{S}_x^{\mathrm{T}} \boldsymbol{S}_y + C_{13}^{v-1} \boldsymbol{S}_x^{\mathrm{T}} \boldsymbol{S}_z \\
&+ C_{21}^{v-1} \boldsymbol{S}_y^{\mathrm{T}} \boldsymbol{S}_x + C_{22}^{v-1} \boldsymbol{S}_y^{\mathrm{T}} \boldsymbol{S}_y + C_{23}^{v-1} \boldsymbol{S}_y^{\mathrm{T}} \boldsymbol{S}_z \\
&+ C_{31}^{v-1} \boldsymbol{S}_z^{\mathrm{T}} \boldsymbol{S}_x + C_{32}^{v-1} \boldsymbol{S}_z^{\mathrm{T}} \boldsymbol{S}_y + C_{33}^{v-1} \boldsymbol{S}_z^{\mathrm{T}} \boldsymbol{S}_z.
\end{aligned} \tag{49}
$$

## Appendix 3

The expressions of the derivatives with respect to $\boldsymbol{q}_e$ in Eq. (25) and Eq. (26) are stated as

$$
\left(\frac{\partial J}{\partial \boldsymbol{q}_e}\right)^{\mathrm{T}} = \boldsymbol{S}_x^{\mathrm{T}}(\widetilde{\boldsymbol{r}}_y \boldsymbol{r}_z) + \boldsymbol{S}_y^{\mathrm{T}}(\widetilde{\boldsymbol{r}}_z \boldsymbol{r}_x) + \boldsymbol{S}_z^{\mathrm{T}}(\widetilde{\boldsymbol{r}}_x \boldsymbol{r}_y) \tag{50}
$$

$$
\left(\frac{\partial I_1}{\partial \boldsymbol{q}_e}\right)^{\mathrm{T}} = 2(\boldsymbol{S}_x^{\mathrm{T}} \boldsymbol{S}_x + \boldsymbol{S}_y^{\mathrm{T}} \boldsymbol{S}_y + \boldsymbol{S}_z^{\mathrm{T}} \boldsymbol{S}_z) \boldsymbol{q}_e \tag{51}
$$

$$
\begin{aligned}
\frac{\partial \boldsymbol{C}^{-1}}{\partial q_e^K} &= -\boldsymbol{C}^{-1} \frac{\partial \boldsymbol{C}}{\partial q_e^K} \boldsymbol{C}^{-1} \\
&= -\boldsymbol{C}^{-1} \left(\frac{\partial \boldsymbol{F}}{\partial q_e^K}\right)^{\mathrm{T}} \boldsymbol{F}^{-\mathrm{T}} - \boldsymbol{F}^{-1} \left(\frac{\partial \boldsymbol{F}}{\partial q_e^K}\right) \boldsymbol{C}^{-1},
\end{aligned} \tag{52}
$$

$$
\left(\frac{\partial C_{IJ}^{-1}}{\partial q_e^K}\right) = \left(\frac{\partial \boldsymbol{C}^{-1}}{\partial q_e^K}\right)_{IJ}, \quad \frac{\partial I_1^e}{\partial \boldsymbol{q}_e} = 2\boldsymbol{q}_e^{\mathrm{T}} \boldsymbol{B} \tag{53}
$$

$$
\frac{\partial \boldsymbol{F}}{\partial q_e^K} = [\, \boldsymbol{S}_x(:,K) \quad \boldsymbol{S}_y(:,K) \quad \boldsymbol{S}_z(:,K) \,] \tag{54}
$$

The derivative matrix of an element in Eq. (30) are expressed as

$$
\begin{aligned}
\boldsymbol{J}_e^{\infty} = & \int_V \frac{\mu^{\infty} H^{-2}}{2 I_{\lim}^{\infty}} \boldsymbol{R}_1^{\mathrm{T}} \left[ J^{-\frac{2}{3}} \left( \frac{\partial I_1}{\partial \boldsymbol{q}_e} \right) - \frac{2}{3} J^{-\frac{5}{3}} \left( \frac{\partial J}{\partial \boldsymbol{q}_e} \right) I_1 \right] \mathrm{d}V \\
& + \int_V \frac{1}{2} \mu^{\infty} H^{-1} \boldsymbol{R}_2 \mathrm{d}V - \int_V \frac{1}{2} \mu^{\infty} H^{-1} \boldsymbol{R}_3 \mathrm{d}V \\
& + \int_V \frac{1}{2} \mu^{\infty} H^{-1} \left[ \frac{10}{9} J^{-\frac{8}{3}} \left( \frac{\partial J}{\partial \boldsymbol{q}_e} \right)^{\mathrm{T}} \left( \frac{\partial J}{\partial \boldsymbol{q}_e} \right) I_1 \right] \mathrm{d}V \\
& + \int_V K^{\infty} (J-1) \frac{\partial}{\partial \boldsymbol{q}_e} \left( \frac{\partial J}{\partial \boldsymbol{q}_e} \right)^{\mathrm{T}} \mathrm{d}V + \int_V K^{\infty} \left( \frac{\partial J}{\partial \boldsymbol{q}_e} \right)^{\mathrm{T}} \left( \frac{\partial J}{\partial \boldsymbol{q}_e} \right) \mathrm{d}V \\
& - \int_V \frac{\varepsilon}{2} (\boldsymbol{E}^{\mathrm{T}} \boldsymbol{C}^{-1} \boldsymbol{E}) \frac{\partial}{\partial \boldsymbol{q}_e} \left( \frac{\partial J}{\partial \boldsymbol{q}_e} \right)^{\mathrm{T}} \mathrm{d}V - \int_V \frac{\varepsilon}{2} J \sum_I \sum_J E_I E_J \frac{\partial}{\partial \boldsymbol{q}_e} \left( \frac{\partial C_{IJ}^{-1}}{\partial \boldsymbol{q}_e} \right)^{\mathrm{T}} \mathrm{d}V \\
& - \int_V \frac{\varepsilon}{2} \sum_I \sum_J E_I E_J \left( \frac{\partial J}{\partial \boldsymbol{q}_e} \right)^{\mathrm{T}} \frac{\partial C_{IJ}^{-1}}{\partial \boldsymbol{q}_e} \mathrm{d}V - \int_V \frac{\varepsilon}{2} \sum_I \sum_J E_I E_J \left( \frac{\partial C_{IJ}^{-1}}{\partial \boldsymbol{q}_e} \right)^{\mathrm{T}} \frac{\partial J}{\partial \boldsymbol{q}_e} \mathrm{d}V,
\end{aligned} \tag{55}
$$

$$
\begin{aligned}
\boldsymbol{R}_1 &= J^{-\frac{2}{3}} \left( \frac{\partial I_1}{\partial \boldsymbol{q}_e} \right) - \frac{2}{3} J^{-\frac{5}{3}} \left( \frac{\partial J}{\partial \boldsymbol{q}_e} \right) I_1, \\
\boldsymbol{R}_2 &= J^{-2/3} \frac{\partial}{\partial \boldsymbol{q}_e} \left( \frac{\partial I_1}{\partial \boldsymbol{q}_e} \right)^{\mathrm{T}} - \frac{2}{3} J^{-\frac{5}{3}} \left( \frac{\partial I_1}{\partial \boldsymbol{q}_e} \right)^{\mathrm{T}} \left( \frac{\partial J}{\partial \boldsymbol{q}_e} \right), \\
\boldsymbol{R}_3 &= \frac{2}{3} J^{-\frac{5}{3}} \left[ \left( \frac{\partial J}{\partial \boldsymbol{q}_e} \right)^{\mathrm{T}} \left( \frac{\partial I_1}{\partial \boldsymbol{q}_e} \right) + \frac{\partial}{\partial \boldsymbol{q}_e} \left( \frac{\partial J}{\partial \boldsymbol{q}_e} \right)^{\mathrm{T}} I_1 \right],
\end{aligned} \tag{56}
$$

$$
\begin{aligned}
\boldsymbol{J}_e^{e} = & \int_V \frac{\mu^{e} H^{-2}}{2 I_{\lim}^{e}} \boldsymbol{R}_{v1}^{\mathrm{T}} \left[ (J^{e})^{-\frac{2}{3}} \left( \frac{\partial I_1^{e}}{\partial \boldsymbol{q}_e} \right) \right] \mathrm{d}V \\
& - \int_V \frac{\mu^{e} H^{-2}}{2 I_{\lim}^{e}} \boldsymbol{R}_{v1}^{\mathrm{T}} \left[ \frac{2}{3} \frac{(J^{e})^{-\frac{5}{3}}}{J^{v}} \left( \frac{\partial J}{\partial \boldsymbol{q}_e} \right) I_1^{e} \right] \mathrm{d}V \\
& + \int_V \frac{1}{2} \mu^{e} H^{-1} \boldsymbol{R}_{v2} \mathrm{d}V - \int_V \frac{1}{2} \mu^{e} H^{-1} \boldsymbol{R}_{v3} \mathrm{d}V \\
& + \int_V \frac{1}{2} \mu^{e} H^{-1} \left[ \frac{10}{9} \frac{(J^{e})^{-\frac{8}{3}}}{(J^{v})^{2}} \left( \frac{\partial J}{\partial \boldsymbol{q}_e} \right)^{\mathrm{T}} \left( \frac{\partial J}{\partial \boldsymbol{q}_e} \right) I_1^{e} \right] \mathrm{d}V \\
& + \int_V K^{e} (J^{e} - 1) \frac{1}{J^{v}} \frac{\partial}{\partial \boldsymbol{q}_e} \left( \frac{\partial J}{\partial \boldsymbol{q}_e} \right)^{\mathrm{T}} \mathrm{d}V \\
& + \int_V K^{e} \frac{1}{(J^{v})^{2}} \left( \frac{\partial J}{\partial \boldsymbol{q}_e} \right)^{\mathrm{T}} \left( \frac{\partial J}{\partial \boldsymbol{q}_e} \right) \mathrm{d}V,
\end{aligned} \tag{57}
$$

$$
\begin{aligned}
\boldsymbol{R}_{v1} &= (J^{e})^{-\frac{2}{3}} \left( \frac{\partial I_1^{e}}{\partial \boldsymbol{q}_e} \right) - \frac{2}{3} \frac{(J^{e})^{-\frac{5}{3}}}{J^{v}} \left( \frac{\partial J}{\partial \boldsymbol{q}_e} \right) I_1^{e}, \\
\boldsymbol{R}_{v2} &= (J^{e})^{-\frac{2}{3}} \frac{\partial}{\partial \boldsymbol{q}_e} \left( \frac{\partial I_1^{e}}{\partial \boldsymbol{q}_e} \right)^{\mathrm{T}} - \frac{2}{3} (J^{e})^{-\frac{5}{3}} \left( \frac{\partial I_1^{e}}{\partial \boldsymbol{q}_e} \right)^{\mathrm{T}} \left( \frac{\partial J}{\partial \boldsymbol{q}_e} \right), \\
\boldsymbol{R}_{v3} &= \frac{2}{3} \frac{(J^{e})^{-\frac{5}{3}}}{J^{v}} \left( \left( \frac{\partial J}{\partial \boldsymbol{q}_e} \right)^{\mathrm{T}} \left( \frac{\partial I_1^{e}}{\partial \boldsymbol{q}_e} \right) + \frac{\partial}{\partial \boldsymbol{q}_e} \left( \frac{\partial J}{\partial \boldsymbol{q}_e} \right)^{\mathrm{T}} I_1^{e} \right),
\end{aligned} \tag{58}
$$

where $H = 1-(J^{-2/3}I_1-3)/I_{\lim}^{\infty}$ and the detailed expressions of the derivatives are written as

$$\begin{aligned}\frac{\partial}{\partial \boldsymbol{q}_e}\left(\frac{\partial J}{\partial \boldsymbol{q}_e}\right)^{\mathrm{T}} &= \boldsymbol{S}_x^{\mathrm{T}}(\widetilde{\boldsymbol{r}}_y\boldsymbol{S}_z)-\boldsymbol{S}_x^{\mathrm{T}}(\widetilde{\boldsymbol{r}}_z\boldsymbol{S}_y)+\boldsymbol{S}_y^{\mathrm{T}}(\widetilde{\boldsymbol{r}}_z\boldsymbol{S}_x)\\ &-\boldsymbol{S}_y^{\mathrm{T}}(\widetilde{\boldsymbol{r}}_x\boldsymbol{S}_z)+\boldsymbol{S}_z^{\mathrm{T}}(\widetilde{\boldsymbol{r}}_x\boldsymbol{S}_y)-\boldsymbol{S}_z^{\mathrm{T}}(\widetilde{\boldsymbol{r}}_y\boldsymbol{S}_x),\end{aligned} \tag{59}$$

$$\frac{\partial}{\partial \boldsymbol{q}_e}\left(\frac{\partial I_1}{\partial \boldsymbol{q}_e}\right)^{\mathrm{T}} = 2(\boldsymbol{S}_x^{\mathrm{T}}\boldsymbol{S}_x+\boldsymbol{S}_y^{\mathrm{T}}\boldsymbol{S}_y+\boldsymbol{S}_z^{\mathrm{T}}\boldsymbol{S}_z) \tag{60}$$

$$\frac{\partial}{\partial \boldsymbol{q}_e}\left(\frac{\partial I_1^e}{\partial \boldsymbol{q}_e}\right)^{\mathrm{T}} = 2\boldsymbol{B}^{\mathrm{T}},\ \left(\frac{\partial^2 C_{IJ}^{-1}}{\partial q_e^M \partial q_e^N}\right) = \left(\frac{\partial^2 \boldsymbol{C}^{-1}}{\partial q_e^M \partial q_e^N}\right)_{IJ} \tag{61}$$

$$\begin{aligned}\frac{\partial^2 \boldsymbol{C}^{-1}}{\partial q_e^M \partial q_e^N} &= -\frac{\partial \boldsymbol{C}^{-1}}{\partial q_e^M}\left(\frac{\partial \boldsymbol{F}}{\partial q_e^N}\right)^{\mathrm{T}}\boldsymbol{F}^{-\mathrm{T}}-\boldsymbol{C}^{-1}\left(\frac{\partial \boldsymbol{F}}{\partial q_e^N}\right)^{\mathrm{T}}\frac{\partial \boldsymbol{F}^{-\mathrm{T}}}{\partial q_e^M}\\ &-\frac{\partial \boldsymbol{F}^{-1}}{\partial q_e^M}\left(\frac{\partial \boldsymbol{F}}{\partial q_e^N}\right)\boldsymbol{C}^{-1}-\boldsymbol{F}^{-1}\left(\frac{\partial \boldsymbol{F}}{\partial q_e^N}\right)\frac{\partial \boldsymbol{C}^{-1}}{\partial q_e^M}.\end{aligned} \tag{62}$$

## Appendix 4

The analytical model for homogeneously deforming DEs is given in appendix 4. Subject to electric field along $\boldsymbol{Z}$ direction, the evolution equation of lateral stretch $\lambda_x$ is written as [38]

$$\dot{\lambda}_x = \frac{\mu^e}{3\eta_v}\frac{(\lambda_x^2\lambda_x^{v-1}-\lambda_x^{-4}\lambda_x^{v5})}{\left(1-\frac{2\lambda_x^2\lambda_x^{v-2}+\lambda_x^{-4}\lambda_x^{v4}-3}{I_{\lim}^{\infty}}\right)} \tag{63}$$

where $\lambda_x^v$ is the viscous stretch obtained from

$$\left(\frac{\varphi_z}{L}\right)^2\frac{\varepsilon}{\mu^{\infty}} = \frac{(\lambda_x^{-2}-\lambda_x^{-8})}{\left(1-\frac{2\lambda_x^2+\lambda_x^{-4}-3}{I_{\lim}^{\infty}}\right)}+\frac{\mu^e}{\mu^{\infty}}\frac{(\lambda_x^{-2}\lambda_x^{v-2}-\lambda_x^{-8}\lambda_x^{v4})}{\left(1-\frac{2\lambda_x^2\lambda_x^{v-2}+\lambda_x^{-4}\lambda_x^{v4}-3}{I_{\lim}^{\infty}}\right)}. \tag{64}$$

## Appendix 5

In appendix 5, the norm of the strain vector of the rolled DEA is defined as

$$\varepsilon = \sqrt{(\varepsilon_x^2+\varepsilon_y^2+\varepsilon_z^2)} \tag{65}$$

where $\varepsilon_x$, $\varepsilon_y$ and $\varepsilon_z$ are the normal strains along $\boldsymbol{X}$, $\boldsymbol{Y}$ and $\boldsymbol{Z}$ directions, respectively, which are given by

$$\varepsilon_x = \frac{1}{2}\left(\boldsymbol{r}_x^{\mathrm{T}}\boldsymbol{r}_x-1\right),\ \varepsilon_y = \frac{1}{2}\left(\boldsymbol{r}_y^{\mathrm{T}}\boldsymbol{r}_y-1\right),\ \varepsilon_z = \frac{1}{2}\left(\boldsymbol{r}_z^{\mathrm{T}}\boldsymbol{r}_z-1\right) \tag{66}$$

## Data availability

Data will be made available on request.

## References

[1] V. Mohammadi, G.S. Mohammadi, M. Tajdani, et al., Evaluating stacked dielectric elastomer actuators as soft motor units for forming artificial muscles in biomimetic rehabilitation robots, Actuators 13 (10) (2024) 381.
[2] A. Li, P. Cuvin, S. Lee, et al., Data -driven long-term energy efficiency prediction of dielectric elastomer artificial muscles, Adv. Funct. Mater. 34 (42) (2024) 2406710.
[3] N. Li, Y. Xue, Y. Li, et al., A soft gripper driven by conical dielectric elastomer actuator to achieve displacement amplification and compliant grips, Intel. Serv. Robot. 17 (5) (2024) 993–1003.
[4] C.R. Kelley, J.L. Kauffman, Towards wearable tremor suppression using dielectric elastomer stack actuators, Smart Mater. Struct. 30 (2) (2020) 025006.

[5] C.T. Nguyen, H. Phung, T.D. Nguyen, et al., A small biomimetic quadruped robot driven by multistacked dielectric elastomer actuators, Smart Mater. Struct. 23 (6) (2014) 1–12.
[6] X. Ma, Y. Wang, W. Zang, et al., Fabrication of multi-layer stacked dielectric elastomer actuator with high output force by co-crosslinking of electrode with DE substrate, Compos. Commun. 47 (2024) 101874.
[7] J. Shintake, S. Rosset, B.E. Schubert, et al., A foldable antagonistic actuator, IEEE/ASME Trans. Mechatron. 20 (5) (2015) 1997–2008.
[8] W.J. Sun, F. Liu, Z.Q. Ma, et al., Soft mobile robots driven by foldable dielectric elastomer actuators, J. Appl. Phys. 12 (8) (2016) 084901.
[9] J. Mersch, M. Koenigsdorff, C.G.G. Nocke, High-speed, helical and self-coiled dielectric polymer actuator, Actuators 10 (1) (2021) 15.
[10] Y. Zhao, Q. Guo, S. Wu, G. Meng, W. Zhang, Design and experimental validation of an annular dielectric elastomer actuator for active vibration isolation, Mech. Syst. Sig. Process. 134 (2019) 106367.
[11] Z. Lai, M. Wu, J. Zhang, et al., A pendulum-type annular dielectric elastomer generator for multi-directional ultra-low-frequency vibration energy harvesting, Mech. Syst. Sig. Process. 220 (2022) 111704.
[12] H. Lewis, M. Pan, Soft end effector using spring roll dielectric elastomer actuators, Actuators 12 (11) (2023) 412.
[13] J. Li, L. Liu, Y. Liu, J. Leng, Dielectric elastomer spring-roll bending actuators: applications in soft robotics and design, Soft Rob. 6 (1) (2019) 69–81.
[14] G.K. Lau, H.T. Lim, J.Y. Teo, Y.W. Chin, Lightweight mechanical amplifiers for rolled dielectric elastomer actuators and their integration with bio-inspired wing flappers Smart Mater, Structures 23 (2) (2014) 025021.
[15] J. Kunze, J. Prechtl, D. Bruch, et al., Design, manufacturing, and characterization of thin, core-free, rolled dielectric elastomer actuators, Actuators 10 (4) (2021) 69.
[16] Z. Huichan, A.M. Hussain, et al., Compact dielectric elastomer linear actuators, Adv. Funct. Mater. 1804328 (2018).
[17] H.L. Zou, Z.C. Deng, H. Zhou, Revisited chaotic vibrations in dielectric elastomer systems with stiffening, Nonlinear Dyn. 110 (1) (2022) 55–67.
[18] Y. Tang, X. Yuan, Z. Zhao, et al., Periodic and chaotic vibrations of dielectric elastomer spherical shells considering structural damping, Nonlinear Dyn. 113 (2) (2025) 1025–1040.
[19] A. Farvandi, A.K. Mohammadi, Nonlinear vibration analysis of hyperelastic and dielectric microbeams with a control parameter using nonlinear normal modes, Nonlinear Dyn. 113 (3) (2025) 2045–2059.
[20] G. Rizzello, M. Hodgins, D. Naso, A. York, S. Seelecke, Modeling of the effects of the electrical dynamics on the electromechanical response of a deap circular actuator with a mass-spring load, Smart Mater. Struct. 24 (9) (2015) 094003.
[21] L. Huaanl, W. Huaming, Y. Youpeng, Static characteristic of dielectric elastomer cylindrical actuator, Trans. Chin. Soc. Agric. Mach. 43 (9) (2012) 202–208.
[22] R. Sarban, B. Lassen, M. Willatzen, Dynamic electromechanical modeling of dielectric elastomer actuators with metallic electrodes, IEEE/ASME Trans. Mechatron. 17 (5) (2012) 960–967.
[23] L.A. Garcia, M.A. Trindade, Finite element modeling and parametric analysis of a dielectric elastomer thin-walled cylindrical actuator, J. Braz. Soc. Mech. Sci. Eng. 41 (1) (2018) 18.
[24] B. Jamin, T.M. Kcy, E. Calius, Finite element modelling of dielectric elastomer minimum energy structure, Appl. Phys. 94 (4) (2009) 507–514.
[25] A.K. Sharma, M.M. Joglekar, A numerical framework for modeling anisotropic dielectric elastomers, Comput. Methods Appl. Mech. Eng. 344 (2019) 402–420.
[26] K. Luo, Q. Tian, H. Hu, Dynamic modeling, simulation and design of smart membrane systems driven by soft actuators of multilayer dielectric elastomers, Nonlinear Dyn. 102 (3) (2020) 1463–1483.
[27] F. Li, Y. Guo, L. Li, D. Zhang, W.H. Liao, Dynamic modeling of a soft robotic fish driven by dielectric elastomer based on the ANCF and IB-LBM, Mech. Syst. Sig. Process. 213 (2024) 111366.
[28] J. Zhang, J. Ru, H. Chen, et al., Viscoelastic creep and relaxation of dielectric elastomers characterized by a Kelvin-Voigt-Maxwell model, Appl. Phys. Lett. 110 (4) (2017) 044104.
[29] Q. Tian, P. Zhang, K. Luo, Dynamics of soft mechanical systems actuated by dielectric elastomers, Mech. Syst. Sig. Process. 151 (2021) 107392.
[30] M. Bozlar, C. Punckt, S. Korkut, et al., Dielectric elastomer actuators with elastomeric electrodes, Appl. Phys. Lett. 101 (9) (2012) 091907.
[31] G. Moretti, G. Rizzello, M. Fontana, S. Seelecke, High-frequency voltage-driven vibrations in dielectric elastomer membranes, Mech. Syst. Sig. Process. 168 (2022) 108677.
[32] X. Zhao, S.J.A. Koh, Z. Suo, Nonequilibrium thermodynamics of dielectric elastomers, Int. J. Appl. Mech. 3 (2) (2011) 203–217.
[33] C.C. Foo, S. Cai, S.J.A. Koh, et al., Model of dissipative dielectric elastomers, J. Appl. Phys. 111 (3) (2012) 836.
[34] A. Khurana, A.K. Sharma, M.M. Joglekar, Nonlinear oscillations of electrically driven aniso-visco-hyperelastic dielectric elastomer minimum energy structures, Nonlinear Dyn. 104 (3) (2021) 1991–2013.
[35] F. Liu, J. Zhou, Shooting and arc-length continuation method for periodic solution and bifurcation of nonlinear oscillation of viscoelastic dielectric elastomers, J. Appl. Mech. 85 (1) (2018) 011005.
[36] D. Eder-Goy, Y. Zhao, B.X. Xu, Dynamic pull-in instability of a prestretched viscous dielectric elastomer under electric loading, Acta Mech. 228 (2017) 4293–4307.
[37] C.C. Foo, S.J.A. Koh, C. Keplinger, et al., Performance of dissipative dielectric elastomer generators, J. Appl. Phys. 111 (9) (2012) 836–839.
[38] A.K. Sharma, M.M. Joglekar, A computationally efficient locking free numerical framework for modeling visco-hyperelastic dielectric elastomers, Comput. Methods Appl. Mech. Eng. 352 (2019) 625–653.
[39] G.Y. Gu, U. Gupta, J. Zhu, et al., Modeling of viscoelastic electromechanical behavior in a soft dielectric elastomer actuator, IEEE Trans. Rob. 33 (5) (2017) 1263–1271.
[40] A. Alibakhshi, H. Heidari, Nonlinear dynamics of dielectric elastomer balloons based on the Gent-Gent hyperelastic model, Eur. J. Mech. A Solids 82 (1) (2020) 103986.
[41] H.L. Li, L.L. Chen, C. Zhao, et al., Evoking or suppressing electromechanical instabilities in soft dielectrics with deformation-dependent dielectric permittivity, Int. J. Mech. Sci. 202–203 (5454) (2021) 106507.
[42] L.J. Liu, Y.C. Han, Z.C. Xing, et al., Nonlinear deformation and instability of a dielectric elastomer tube actuator, Int. J. Non Linear Mech. 147 (7) (2022) 104235.
[43] K. Mrabet, E. Zaouali, F. Najar, Internal resonance and nonlinear dynamics of a dielectric elastomer circular membrane, Int. J. Solids Struct. 236–237 (10) (2021) 111338.
[44] D.L. Henann, S.A. Chester, K., Modeling of dielectric elastomers: Design of actuators and energy harvesting devices, J. Mech. Phys. Solids 61 (10) (2013) 2047–2066.
[45] R. Mao, B. Wu, E. Carrera, et al., Electrostatically tunable small-amplitude free vibrations of pressurized electro-active spherical balloons, Int. J. Non Linear Mech. 117 (2019) 103237.